Lawrence Berkeley National Laboratory
LBL Publications

Title
The Evolution of Magnetism in a Thin Film Pyrochlore Ferromagnetic Insulator

Permalink
https://escholarship.org/uc/item/58b4g4w0

Journal
Advanced Functional Materials, 36(81)

ISSN
1616-301X

Authors
Anderson, Margaret A
Goh, Megan E
Zhang, Yang
et al.

Publication Date
2026-10-01

DOI
10.1002/adfm.202522413

Copyright Information
This work is made available under the terms of a Creative Commons Attribution License, available at https://creativecommons.org/licenses/by/4.0/

Peer reviewed

eScholarship.org Powered by the California Digital Library
University of California

arXiv:2603.05717v1 [cond-mat.mtrl-sci] 5 Mar 2026

The evolution of magnetism in a thin film pyrochlore ferromagnetic insulator

Margaret A. Anderson*,[1] Megan E. Goh*,[2] Yang Zhang,[3] Kyeong-Yoon Baek,[1] Michael Schulze,[4] Mario Brützam,[4] Christoph Liebald,[5] Chris Lygouras,[6] Dan Ferenc Segedin,[1] Aaron M. Day,[2] Zubia Hasan,[1] Donald Walko,[7] Hua Zhou,[7] Peter Bencok,[8] Alpha T. N'Diaye,[9] Charles M. Brooks,[1] Ismail El Baggari,[3] John T. Heron,[10] Sayed Koopayeh,[11,12,13] Daniel Rytz,[5] Christo Guguschev,[4] and Julia A. Mundy[1,2]

[1]*Department of Physics, Harvard University, Cambridge, MA, USA*
[2]*School of Engineering and Applied Sciences, Harvard University, Cambridge, MA, USA*
[3]*The Rowland Institute at Harvard, Cambridge, MA, USA*
[4]*Leibniz Institute for Crystal Growth, Max-Born-Str. 2, D-12489 Berlin, Germany*
[5]*EOT GmbH – Coherent, Struthstr. 2, D – 55743 Idar-Oberstein, Germany*
[6]*Institute for Quantum Matter and Department of Physics and Astronomy, Johns Hopkins University, Baltimore, MD, USA*
[7]*X-ray Science Division, Advanced Photon Source, Argonne National Laboratory, Lemont, IL, USA*
[8]*Diamond Light Source, Didcot, Oxfordshire, OX11 0DE, United Kingdom*
[9]*Advanced Light Source, Lawrence Berkeley National Laboratory, Berkeley, CA, USA*
[10]*Department of Materials Science and Engineering, University of Michigan, Ann Arbor, MI, USA*
[11]*Institute for Quantum Matter and Department of Physics and Astronomy, Johns Hopkins University, Baltimore, MD, USA*
[12]*Department of Materials Science and Engineering, Johns Hopkins University, Baltimore, MD, USA*
[13]*Ralph O'Connor Sustainable Energy Institute, Johns Hopkins University, Baltimore, MD, USA*

The pyrochlore vanadates are compelling candidates for next-generation dissipationless devices. $Lu_2V_2O_7$ and $Y_2V_2O_7$ are ferromagnetic insulators ($T_c \sim 70$ K) that are believed to exhibit the magnon Hall effect and are expected to host topological magnons. Their completely dissipationless magnon edge states could be harnessed to realize low-power information transport in spintronic or magnonic devices. As a crucial step in the realization of devices, we synthesize the first thin films of pyrochlore $Y_2V_2O_7$ on isostructural $Y_2Ti_2O_7$ substrates and explore the evolution of their magnetic properties down to the ultrathin limit. All films are insulating ferromagnets with transition temperatures of up to the bulk value ($T_c \sim 68$ K) that decrease with thickness according to finite-size effects. Our films also exhibit a change in anisotropy from in-plane to out-of-plane easy axis coincident with the development of partial strain relaxation and nonzero magnetic hysteresis in an applied field. This evolution demonstrates the impact of strain on magnetic anisotropy and paves the way to tunable magnon topology.

I. INTRODUCTION

The ferromagnetic insulating pyrochlore vanadates ($A_2V_2O_7$, A = Y, Lu) are promising platforms for low-power spintronic [1–3] or magnonic [3–7] devices. In addition to interest as ferromagnetic insulators ($T_c \sim 70$ K) [1, 3, 8–11], the vanadate pyrochlores are predicted to host topological magnons with fully dissipationless magnon transport in edge states [2, 5–7, 12]. This nontrivial topology of magnons leads $Lu_2V_2O_7$ to exhibit the magnon hall effect [3, 4, 12–14] and suggests that the pyrochlore vanadates can transport information in the form of edge-confined, topologically-protected spin waves in low-power magnon-based devices.

The vanadates belong to a family of isostructural materials, the pyrochlore oxides, with generic formula $A_2B_2O_6O'$ where both the A and B cations form separate but interpenetrating sublattices of corner sharing tetrahedra (Figure 1a) often called the pyrochlore sublattice [15]. This sublattice, the 3D analog of the Kagome lattice, is geometrically frustrated. In $A_2V_2O_7$, V^{4+} ($3d^1$, $s = \frac{1}{2}$) sits in a nearly octahedral oxygen coordination environment with a slight trigonal distortion that splits the lower energy T_{2g} states of the octahedral environment into a lowest lying A_{1g} state and higher energy doubly-degenerate E'_g states (Figure S1) [1, 10, 16, 17]. In this configuration, the V^{4+} ions host isotropic Heisenberg exchange and weak but nontrivial Dzyaloshinskii-Moriya (DM) superexchange allowed by Moriya's rules and enabled by spin-orbit coupling [4, 10, 14, 18, 19]. From this relatively simple model on the pyrochlore lattice, myriad unexpected properties emerge. $Y_2V_2O_7$ and isostructural $Lu_2V_2O_7$ are ferromagnetic insulators contrary to the expectation that the unpaired spins leading to a net magnetic moment should produce a metallic state [1, 8–10]. The collinear ferromagnetism is thought to be stabilized by orbital order leading to nontrivial higher-order electron hopping [20] or via thermal order-by-disorder that selects a subset of spin configurations from an O(3) manifold of degenerate states [21]. Although the DM interaction cancels out across nearest-neighbor bonds, preserving the collinear spin arrangement [4, 7, 21], the fictitious magnetic flux caused by ring exchange about inequivalent loops in the pyrochlore structure enables topological magnon edge states and the magnon Hall effect [12–14]. $Lu_2V_2O_7$ powder exhibits a light-induced metal-to-insulator transition [8] while sin-

gle crystals show colossal magnetoresistance near the ferromagnetic transition temperature. Theoretical studies suggest device applications of pyrochlore vanadates ranging from a field-induced spin transistor [1] to a topological magnon waveguide [6].

Early efforts to synthesize single crystals of the $Y_2V_2O_7$ yielded micron-scale crystallites embedded in a matrix of unreacted starting material [11, 22]. Higher-quality floating zone single crystals of $Lu_2V_2O_7$ enabled the observation of orbital ordering [17], ferromagnetic-cluster-mediated colossal magnetoresistance [23], and the first observation of the magnon Hall effect [4]. Recently, macroscopic single crystals of $Y_2V_2O_7$ have been reported as well [3]. While single crystals are ideal for thermal transport and neutron scattering measurements, the thin film geometry is key to realizing practical devices. In addition to enabling device fabrication and integration, thin film synthesis offers a variety of pathways to modify and improve the functionality of materials. Film properties can be tuned with epitaxial strain, modulated doping, and interfacial effects [24, 25]. In thin films of $Y_2V_2O_7$, strain and dimensional confinement could modify the strength of magnetic exchange and tune the ferromagnetic ordering [2] or magnetic anisotropy, thereby impacting the topological magnon states [6, 7, 12, 26, 27].

Here, we synthesize the first thin films of $Y_2V_2O_7$ and characterize their magnetic properties as a function of thickness, strain, and dimensional confinement. We further take advantage of the Kagome-triangular plane layering in the [111] direction (Figure 1a) of the pyrochlore structure and the atomic precision of molecular beam epitaxy to isolate sub-unit-cell thicknesses and explore the unusual ferromagnetism of $Y_2V_2O_7$ in the ultrathin limit. We find that our high-quality thin films of pyrochlore $Y_2V_2O_7$ exhibit the ferromagnetic insulating state found in bulk crystals down to sub-unit-cell thicknesses. However, the Curie temperature of the films decreases in thinner films following finite-size effects. The thin films exhibit hysteresis under an applied field with a coercivity that increases with thickness. Finally, the $Y_2V_2O_7$ shows a change in anisotropy coincident with the onset of partial relaxation in thicker films and counter to fundamental expectations based on shape and surface anisotropy. Understanding the interplay of dimensionality, strain, and magnetism in these films is critical to the fabrication and realization of magnonic devices and sheds light on the intersection of topology and frustration in thin films writ large.

II. RESULTS

A. Synthesis and Structural Characterization

Using reactive-oxide molecular beam epitaxy (MBE), we realize the first thin films of pyrochlore $Y_2V_2O_7$ on the isostructural substrate $Y_2Ti_2O_7(111)$. YVO_x on yttria-stabilized zirconia (YSZ) substrates forms a phase with pyrochlore-like reflection high energy electron diffraction (RHEED) and x-ray diffraction (XRD) patterns that indicate the expected doubling of the out-of-plane lattice parameter of the film compared to the substrate (Figure S2). However, magnetic susceptibility measurements yield $T_c \approx 140$ K; twice as high as expected from bulk $Y_2V_2O_7$ crystals (Figure S3). Subsequently, high-angle annular dark field scanning transmission electron microscopy (HAADF-STEM) imaging reveals a non-pyrochlore phase with alternating 111 planes, but no discernible in-plane order (Figure S4). Based on the film's fast Fourier transform (FFT) and comparison with the diffraction patterns of defect fluorite and pyrochlore crystals, we identify the phase as an anisotropic defect fluorite with pyrochlore-like ordering in the 111 direction. While this phase may be of interest as a highly insulating high-T_c ferromagnetic insulator, it lacks the 111 vanadium kagome planes that lead to nontrivial magnon topology in $Y_2V_2O_7$. Therefore films on YSZ are not promising platforms for low dissipation magnonic devices.

Moving away from the more common YSZ substrate, we successfully stabilize pyrochlore $Y_2V_2O_7$ films on non-commercial $Y_2Ti_2O_7$ pyrochlore substrates (Figure S5). In situ RHEED indicates smooth, highly crystalline films (Figure S6). Atomic force microscopy confirms that the film surfaces are atomically smooth with RMS roughness on the order of 150 pm (Figure S7). As on YSZ, XRD exhibits the expected pyrochlore peaks with thickness fringes that are a further testament to film quality (Figure 1b and Figure S8). HAADF-STEM imaging shows an exceptionally high-quality film, nearly indistinguishable from the isostructural substrate, with the ideal checkerboard-like cation ordering of a pyrochlore viewed along $\langle 1\bar{1}0\rangle$ (Figure 1c and Figure S9). The film exhibits minimal cation disorder and no extended defects, such as antiphase boundaries that are common to pyrochlore thin films on YSZ substrates [28]. Atomic resolution electron energy loss spectroscopy (EELS) mapping of elemental concentration further presents a well-ordered pyrochlore film atop a sharp substrate-film interface with at most one monolayer of interdiffusion (Figure 1d and Figure S10). Both EELS and x-ray absorption spectroscopy (XAS) measurements of the V-$L_{2,3}$ edge show the expected peak shape for V^{4+} in a nearly octahedral coordination environment.

Based on the lattice mismatch between $Y_2V_2O_7$ and $Y_2Ti_2O_7$, fully strained films experience approximately 0.9% tensile strain. Reciprocal space mapping shows that our $Y_2V_2O_7$ films are fully strained up to at least 45 atomic layers (12.8 nm). Beyond this critical thickness, films show partial relaxation indicated by a diffuse background spread towards the bulk $Y_2V_2O_7$ peak position (Figure S11).

To probe the magnetic properties at the ultrathin limit of $Y_2V_2O_7$, we leverage the atomic layer precision of MBE to synthesize a series of $(Y_2Ti_2O_7)_m/(Y_2V_2O_7)_n$ superlattices where $m, n \in \mathbb{N}$ are the number of atomic planes in each repeat. Superlattices enable the charac-

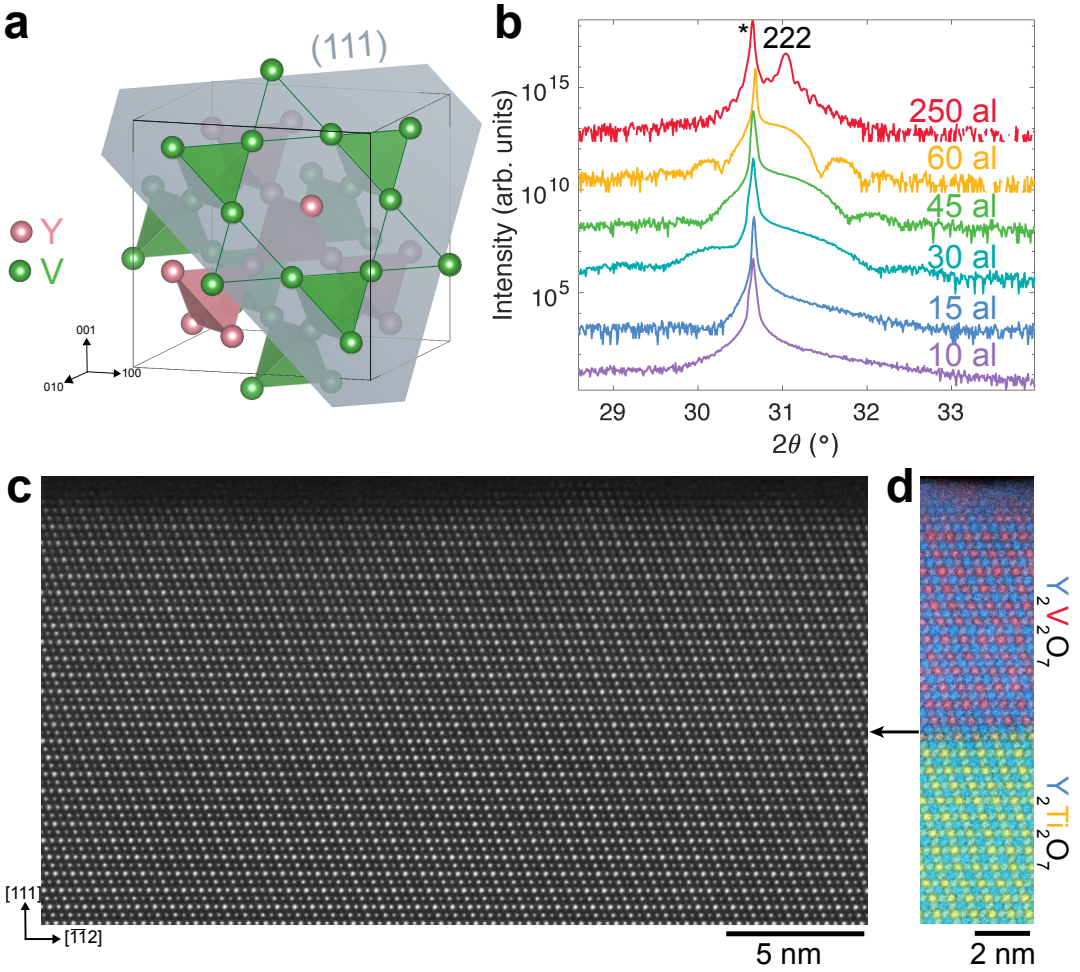


FIG. 1. Pyrochlore structure and characterization. **a** The cation structure of $Y_2V_2O_7$ showing the separate interpenetrating pyrochlore sublattices of corner sharing tetrahedra and an isolated 111 vanadium Kagome plane **b** X-ray diffraction about the 222 substrate ($Y_2Ti_2O_7$, denoted by asterisk) and film ($Y_2V_2O_7$) for the thickness series (al = atomic layers) showing thickness fringes indicative of smooth, high-quality films **c** HAADF-STEM micrograph of the 30 atomic layer $Y_2V_2O_7$ film along $\langle 1\bar{1}0\rangle$ showing nearly indistinguishable interface between substrate and film **d** An EELS micrograph of the same film as (c) at approximately the same scale showing a clear interface between film (top) and substrate (bottom)

terization of the magnetic properties of the film in the ultrathin limit by maintaining the low dimensionality while increasing the total magnetic signal produced by multiple non-interacting repeats. While these samples allow us to avoid sample volume limits for our magnetic measurements, some prior studies have suggested that interlayer coupling can have an effect on magnetic properties [29, 30]. We thus label each data point in magnetic data that arises from superlattice samples. In each superlattice, we hold $m = 6$ so that each nonmagnetic $Y_2Ti_2O_7$ is a full unit cell thick to ensure negligible interlayer coupling between $Y_2V_2O_7$ layers: the magnetic exchange interaction is known to be vanishingly small beyond the nearest neighbors [18]. We vary $n \in \{2, 6, 10\}$ to compare directly with the thickness series and smoothly probe unit-cell and single tetrahedra thicknesses (Figure S12). We adjust the number of superlattice repeats to maintain 30 total atomic layers of $Y_2V_2O_7$ to ensure a measurable magnetic signal. To confirm our measurements are not dominated by the effects of interdiffusion, we further synthesized a set of fully disordered $Y_2Ti_xV_{2-x}O_7$ samples with the same Ti:V ratio and overall thickness.

In situ RHEED shows the superlattices are smooth and highly crystalline, similar to single phase $Y_2V_2O_7$ or $Y_2Ti_2O_7$ films. Due to the similar atomic weight of titanium and vanadium, the superlattice layering is challenging to characterize with diffraction techniques (Figure S13). Only the $(Y_2Ti_2O_7)_6/(Y_2V_2O_7)_6$ superlattice shows a single weak XRD satellite peak about the 222 film peak near the expected superlattice peak position. This peak is absent in the corresponding Y_2TiVO_7 film. The low noise floor of synchrotron XRD more clearly reveals this presumed superlattice peak and confirms the absence of defect phases (Figure S14). STEM imaging

shows the superlattice forms the pyrochlore structure with minimal A-B site cation disorder (Figure S15) while atomic resolution EELS maps of vanadium and titanium concentration show increasing interdiffusion deeper in the film (Figure S16).

B. Magnetic Properties

All films are ferromagnetic insulators like bulk $Y_2V_2O_7$ and $Lu_2V_2O_7$. $Y_2V_2O_7$ films show a high surface resistance that increases in thinner films. Resistivity versus temperature shows fully insulating behavior (Figure S17). Magnetic susceptibility measurements of the thickest $Y_2V_2O_7$ film in a 500 Oe in-plane applied field reproduces the bulk crystal susceptibility behavior with a sharp ferromagnetic transition at $T_c = 67 \pm 3$ K and a plateau at low temperatures (Figure 2a, red). The field-cooled and zero-field curves diverge below T_c (Figure S18). Fitting the high temperature inverse susceptibility to the Curie-Weiss law yields $\theta_{CW} \approx 69$ K and $\mu_{eff} \approx 1.83\ \mu_B$/V atom (Figure S19). For thinner films, the qualitative susceptibility behavior remains the same (Figure 2a and Figure S20) however the ferromagnetic T_c decreases following the finite-size effect:

$$T_c(n) = An^{-B} + C, \tag{1}$$

where $B = 1$ for a simple mean-field theory and C is the bulk Curie temperature [31]. The fit of this function to the measured T_c of $Y_2V_2O_7$ films with thicknesses ranging from about 10-250 atomic layers (Figure 2b) yields a scaling factor $B = 0.93$, similar to that expected from mean-field theory, and $C = 67.7$ K, consistent with the bulk Curie temperature $T_{c,bulk} = 68$ K [3, 11]. The superlattice transition temperatures also align well with an extrapolation of the finite-size fit, suggesting that T_c approaches 0 K in the monolayer limit, in contrast to theoretical predictions that the ferromagnetic transition temperature may be enhanced to room temperature or above in few monolayer films of the pyrochlore vanadates (Figure S21) [2].

X-ray magnetic circular dichroism measurements at the V-$L_{2,3}$ edge of a 60 atomic layer $Y_2V_2O_7$ film begins to show a signal near the ferromagnetic transition temperature ($T_c \sim 61$ K) of susceptibility measurements (Figure S22). This confirms that the ferromagnetism arises from the V^{4+} ions, as expected.

As hinted by the splitting of the field-cooled and zero-field-cooled susceptibility below the transition temperature, the magnetization of the thickest (250 atomic layer) film shows hysteresis under an applied field (Figure 3a, red). The narrow coercive field (at most 133 ± 7 Oe at 1.8 K) confirms that thin films of $Y_2V_2O_7$ behave as soft ferromagnets like fully oxidized bulk crystals of both $Lu_2V_2O_7$ and $Y_2V_2O_7$, which lack measurable hysteresis entirely [3, 32]. The hysteresis persists largely unchanged in films of approximately 60 atomic layers (Figure 3a,b). In thinner films, the coercivity shrinks approaching the ultrathin limit (Figure 3c and Figure S26). In magnetic thin films, coercivity tends to increase in the thinnest films as increasing strain induces defects, which act as pinning sites for magnetic domain walls [33]. Here, the growth in coercivity accompanies partial relaxation as film thickness increases past the critical value determined with RSM. This suggests that the 0.9% tensile strain induced by the slightly larger $Y_2Ti_2O_7$ stabilizes the defect-free pyrochlore phase while relaxation leads to the formation of defects. A similar effect occurs in Ni/Cu thin films as the nickel thickness is increased past the critical value, leading to relaxation [34]. In all films, the saturation magnetization is on the order of 1 μ_B per vanadium atom as expected for a collinear d^1 ferromagnet. The small volumes of the films lead to sizable uncertainty in the conversion to μ_B/V, which complicates precise interpretation of the saturation value and direct comparison between films. However, the consistent magnitude throughout the thickness series suggests film quality does not degrade significantly down to at least 15 atomic layers. The $n = 10$ superlattice exhibits a larger saturated magnetization than the 10 atomic layer $Y_2V_2O_7$ film, indicating the high quality of the vanadate layers within the superlattice (Figure S27). As n decreases, the magnetic moment decreases until no signal is measured in the $n = 2$ film even at 1.8 K, as expected from the vanishing T_c.

Comparing the magnetization in a field applied within the plane of the film (perpendicular to $\langle 111 \rangle$) and out-of-plane (along $\langle 111 \rangle$), the magnetically easier axis transitions from out-of-plane in the thickest films to in-plane for films below 45 atomic layers thick (Figure 4a-e). This transition is coincident with both the onset of partial strain relaxation and the development of measurable ferromagnetic hysteresis. Accordingly, in films that exhibit this partial relaxation (60 and 250 atomic layers, Figure 4a,b), the out-of-plane magnetization conforms to the in-plane behavior at low fields. This indicates that the relaxed portion of the film may have distinct anisotropy. This change in anisotropy in partially relaxed films can also be seen in XMCD signal measured at normal and grazing incidences (Figures S23-S25). A change in easy axis represents a change of anisotropy, which can be quantified by an anisotropy constant defined as $\Delta M_r/M_s = (M_{r,IP} - M_{r,OOP})/M_s$. Here, due to the uncertainty in the exact value of the magnetic moment between films, we take M_s to be the bulk value, 1 μ_B/V^{4+} ion. Quantifying the anisotropy in our films, we see a transition from positive (in-plane easy axis) towards negative (out-of-plane) anisotropy between the 45 and 60 atomic layer films (Figure 4f), as expected. Full characterization of magnetic behavior of the $Y_2V_2O_7$ thickness series in an out-of-plane field is presented in supplementary figure S28-S30. The $n = 10$ superlattice shows a strong in-plane easy axis (Figure S31). The anisotropy is less dramatic in the $n = 6$ superlattice, possibly due to the effects of interdiffusion.

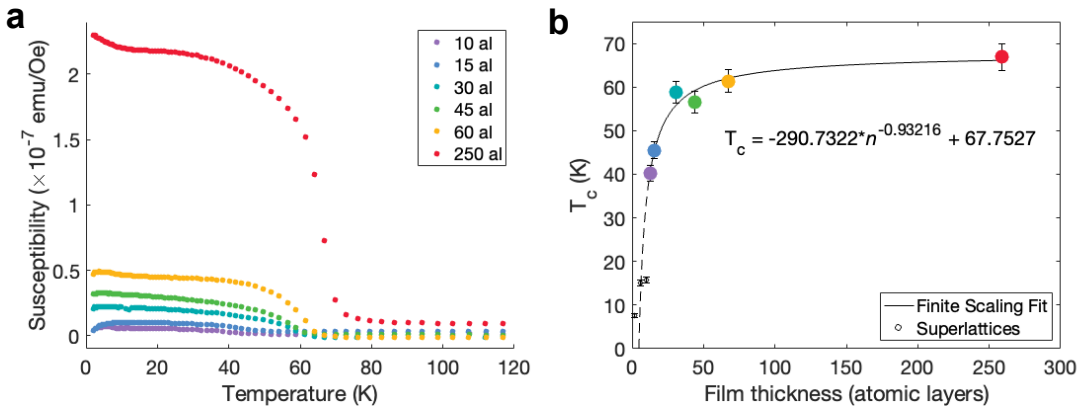


FIG. 2. Magnetic susceptibility of $Y_2V_2O_7$ thickness series. **a** Field-cooled magnetic susceptibility measured in a field of 500 Oe perpendicular to ⟨111⟩ for each sample in the thickness series **b** Ferromagnetic transition temperature vs film thickness (n, atomic layers) with a finite-size scaling fit (solid line, extrapolated along dotted line) that shows excellent agreement with both thickness series (filled circles) and superlattice samples (open circles)

III. DISCUSSION AND CONCLUSION

We explore magnetism in ultrathin films of the pyrochlore ferromagnetic insulator $Y_2V_2O_7$. An important step towards the development of low-power magnonic devices, we synthesize the first reported vanadate pyrochlore thin films. While films on isostructural $Y_2Ti_2O_7$ substrates readily form the pyrochlore phase, YVO_x deposited on commercial YSZ(111), a popular substrate for thin film pyrochlore synthesis, forms a distinct defect phase, which lacks the kagome vanadium planes that lead to nontrivial magnon topology. $Y_2Ti_2O_7$, in contrast, forms the pyrochlore phase on YSZ(111) and may be used as a buffer layer to seed pyrochlore $Y_2V_2O_7$ films. Based on structural characterization with in situ RHEED, XRD, and HAADF-STEM imaging, our films on $Y_2Ti_2O_7$ substrates are higher quality than most bulk crystal $Y_2V_2O_7$ [11, 22]. The films, especially those that are fully strained, are smooth, highly crystalline, and single phase with very little cation disorder. $(Y_2Ti_2O_7)_6/(Y_2V_2O_7)_n$ superlattices are similarly high quality with respect to to strain and pyrochlore structure. However, marked interlayer cation diffusion within these samples may affect their magnetism, and although they display higher ferromagnetic ordering temperatures than their fully disordered counterparts (Figure S21), further superlattice studies are needed to determine whether these samples can fully allow us to probe magnetism down to a two atomic layer ($n = 2$) limit.

The magnetic properties of the thickest film (88 nm, approximately 250 atomic layers) largely reproduce the behavior of bulk crystals. A Curie-Weiss fit of the inverse susceptibility yields a μ_{eff} of 1.83 μ_B per vanadium ion, which is fairly consistent with the theoretical free ion value, 1.73 μ_{eff}, and that found from fitting the inverse susceptibility of $Lu_2V_2O_7$ bulk crystals, 1.75 to 1.89 μ_{eff} per vanadium [8, 11, 23, 35]. The overestimation of this value derives from spin orbit coupling [35]. Our fit also gives a θ_{CW} of 69 K, consistent with the ferromagnetic transition temperature determined by the maximum rate of change of the susceptibility. Intriguingly, all Curie-Weiss fits to bulk crystal $Lu_2V_2O_7$ data yield a θ_{CW} about 30 K higher than the true Curie temperature and show a deviation from linear Curie-Weiss behavior at 130 – 170 K, which is attributed to the formation of ferromagnetic clusters or magnetic polarons above the true ferromagnetic transition [8, 16, 23, 32, 35]. The $Y_2V_2O_7$ thin film, in contrast, conforms well to linear Curie-Weiss behavior down to the ferromagnetic transition temperature, which suggests the formation of ferromagnetic clusters is absent or suppressed.

As film thickness decreases, the measured Curie temperature falls according to finite-size effects with a scaling factor similar to that expected from mean-field theory. Unfortunately, our results suggest that the T_c of ultrathin pyrochlore vanadates will not approach room temperature as hoped [2]. However, further exploration of the pyrochlore-like defect phase that forms on YSZ (with $T_c \approx 140$ K) may suggest pathways to enhance the ferromagnetic transition temperature in $Y_2V_2O_7$ films. Apart from the decay of T_c with decreasing thickness, our films also exhibit magnetic hysteresis that manifests as the films begin to relax. The partial relaxation of films beyond the critical thickness may be accompanied by the formation of defects, which act as domain wall pinning sites. This behavior, also noted in Ni/Cu thin films [34], is contrary to the typical behavior of thin films that form defects to relieve increasing strain. We also find a consistent saturation magnetization of about 0.75 μ_B per vanadium atom for all films, which suggests that the crystal quality of the films is maintained throughout the thickness series down at least 15 atomic layers.

Questions about magnetic anisotropy in the pyrochlore vanadates have attracted significant interest because of their potential impact on magnon transport. Disagreement about the strength of Dzyaloshinskii-Moriya

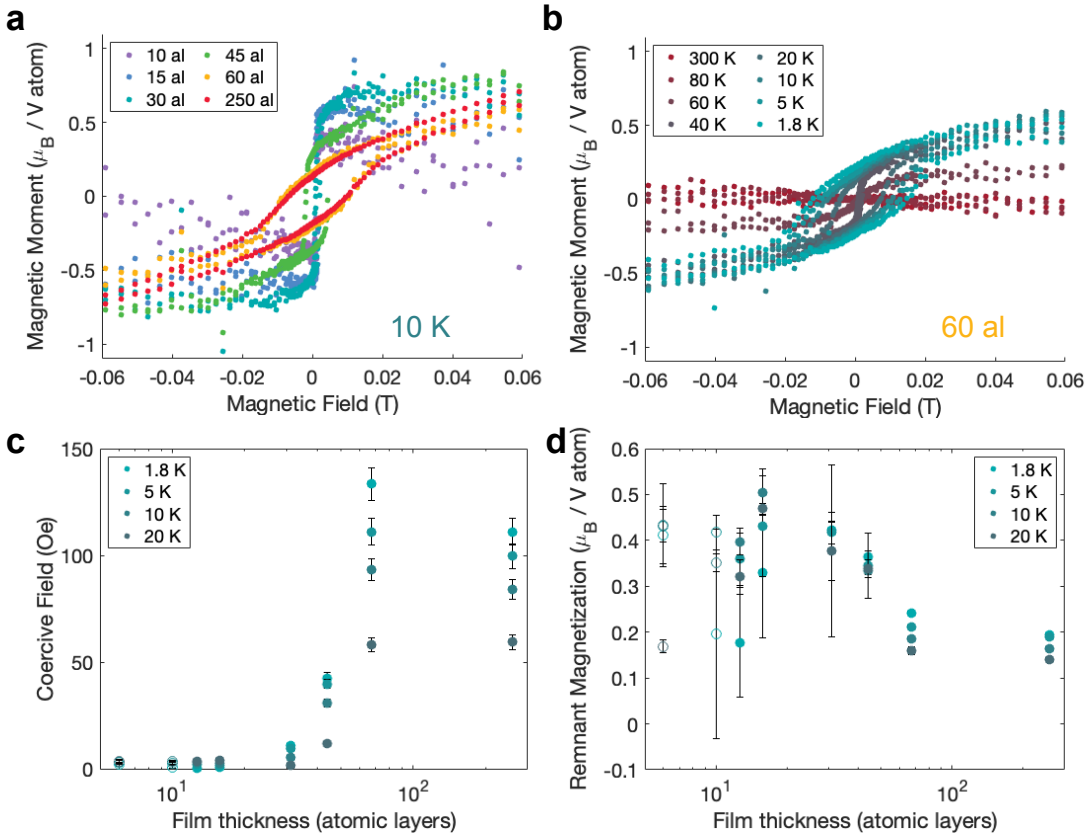


FIG. 3. Magnetization vs. applied field loops. **a** Thickness dependence of magnetization vs. applied field loops measured at 10 K with field perpendicular to ⟨111⟩ **b** Temperature dependence of magnetization vs. applied field loops with field perpendicular to ⟨111⟩ for 60 atomic layers of $Y_2V_2O_7$, which has $T_c = 63$ K **c** Coercive field (width) of magnetization loops vs film thickness and temperature with single-phase films (filled circles) and superlattices (open circles) **d** Remnant magnetization of $Y_2V_2O_7$ thin films vs. thickness and temperature

(DM) interactions led to the suggestion that V^{4+} in the pyrochlore structure possess significant single-ion anisotropy [10, 16], contrary to the fact that such a term should be trivially proportional to identity in a quantum spin-1/2 system [19]. Neutron inelastic scattering suggests that magnetic exchange is largely isotropic in $Lu_2V_2O_7$ [18], though fits to magnetic susceptibility may indicate a change in anisotropy below 170 K [16] or the ferromagnetic Curie temperature [35]. Higher order anisotropic exchange is alternately determined to be non-negligible [19] or dismissed as perturbatively small [21]. Regardless, anisotropy is critically important to the topological behavior of magnons in the pyrochlore vanadates [7, 12, 20] and may be modified in thin films via strain, doping, or dimensionality [7].

In thin films, we see a marked transition of anisotropy that accompanies the onset of partial relaxation between films of about 45 and 60 atomic layers. In thicker films, the magnetically easier axis lies in the out-of-plane 111 direction. At about 45 atomic layers thick, the easy axis transitions to within the plane of the film, partial relaxation occurs, and hysteresis opens. This change in anisotropy is opposite of that expected based on shape anisotropy in the thin film geometry where the thinnest films should exhibit an out-of-plane easy axis to reduce demagnetizing effects [36]. Bulk $Lu_2V_2O_7$ hosts a 100 magnetic easy axis [4], while theoretical studies suggest that individual V^{4+} ions have an easy axis along 111 [10, 16, 21]. We see unique behavior that suggests strain may indeed modify magnetic anisotropy and therefore impact magnon topology in thin films of $Y_2V_2O_7$. The tensile strain may distort the nearly octahedral coordination environment about vanadium atoms, leading to a change in inter- and intralayer exchange interactions and thus the overall magnetic anisotropy [7]. Future explorations of the magnetism of vanadate pyrochlore thin films under strain may open the door to tunable anisotropy and magnon topology and selection of ideal properties for fully dissipationless magnonic devices.

IV. METHODS

The $Y_2Ti_2O_7$ substrate crystal growth was performed using a conventional RF-heated Czochralski setup equipped with a crucible balance. The crystal was grown

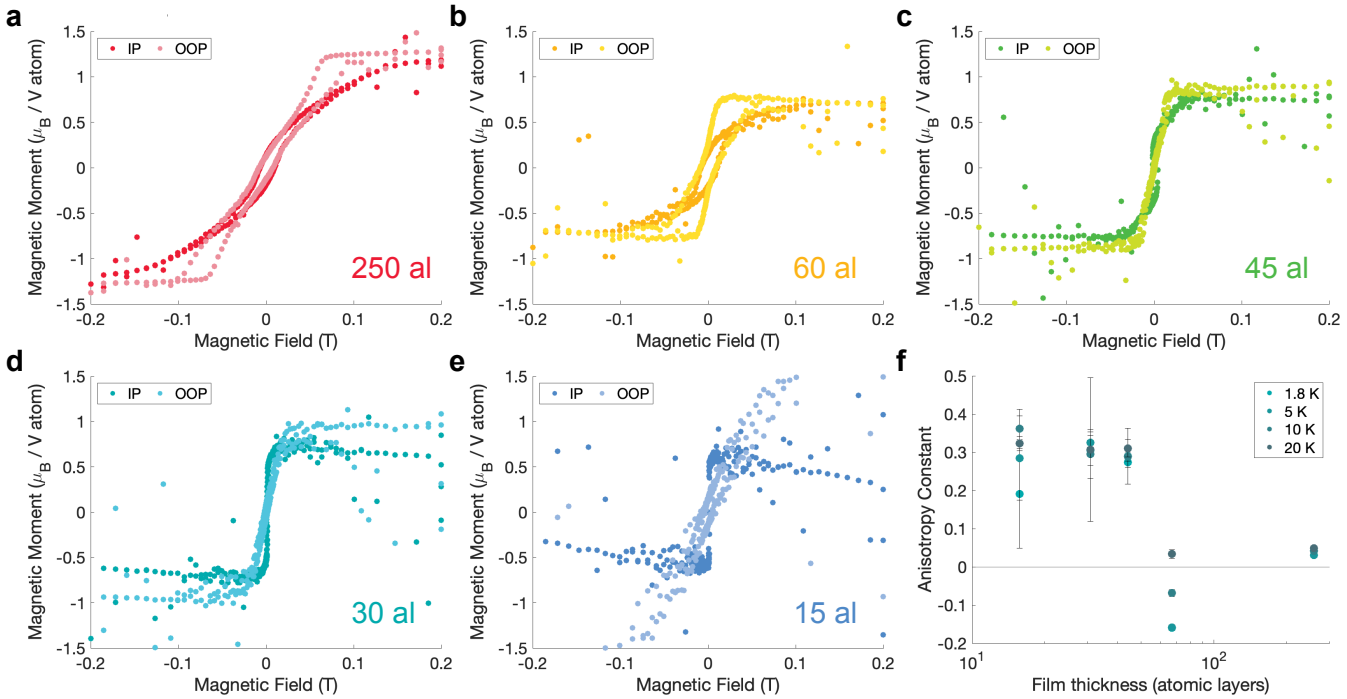


FIG. 4. Magnetic anisotropy of $Y_2V_2O_7$ thin films. **a-e** Magnetization vs. applied field loops at 10 K for a field applied within the plane of the film (IP, perpendicular to ⟨111⟩) and out-of-plane (OOP, field along ⟨111⟩) for films with thickness (a) 250, (b) 60, (c) 45, (d) 30, and (e) 15 atomic layers **f** The anisotropy constant $\Delta M_r = M_{r,IP} - M_{r,OOP}$, assuming constant 1 μ_B saturation, showing a change in anisotropy between the 45 and 60 atomic layer films

by the top-seeded solution growth technique (TSSG) using a flux based on TiO_2 and BaB_2O_4 at an initial melt temperature of about 1600°C. An iridium crucible (about 58 mm inner diameter) embedded in ZrO_2 and Al_2O_3 insulation was used. An actively heated iridium afterheater and a lid with an opening for the seed holder were placed on top of the crucible. The growth of the crystal occurred at a rate of 0.35 mm·h^{-1} using automatic diameter control and a rotation rate of 10 rpm. An Ar/O_2 gas mixture (0.93% O_2) at atmospheric pressure was used as growth atmosphere. Substrates of various sizes were prepared by CrysTec GmbH (Berlin, Germany) from the grown crystals.

We synthesize pyrochlore $Y_2V_2O_7$ thin films and $(Y_2Ti_2O_7)_m/(Y_2V_2O_7)_n$ superlattices with reactive-oxide molecular beam epitaxy in a Riber C21 dual chamber system. Yttrium, titanium, and vanadium are evaporated from elemental sources with fluxes of approximately 10^{12} $\frac{\text{atoms}}{\text{cm}^2\cdot\text{s}}$ roughly calibrated in situ with a quartz crystal microbalance (Figure S7 and S32). YVO_x deposited on $(111)(ZrO_2)_{0.905}(Y_2O_3)_{0.095}$ (yttria-stabilized zirconia or YSZ) forms a pyrochlore-like defect phase (Figure S2-S4). The true pyrochlore phase forms on noncommercial, isostructural $Y_2Ti_2O_7(111)$ substrates at 800°C in 2 × 10^6 torr O_2. Film crystallinity and surface morphology are monitored and optimized with in situ reflection high-energy electron diffraction (RHEED).

Based on a monolayer deposition time inferred from RHEED intensity oscillations and ex-situ x-ray reflectivity measurements of calibration samples, we synthesize a series of pyrochlore $Y_2V_2O_7$ films simultaneously on YSZ(111) and $Y_2Ti_2O_7(111)$ with thicknesses ranging from 10-260 atomic layers (1.67-43.33 unit cells). We first explore proof-of-concept pyrochlore superlattice growth of high atomic contrast $(Y_2Ti_2O_7)_m/(Tb_2Ti_2O_7)_n$ films on YSZ(111) (Figure S33). We then synthesize a set of superlattices with 6 atomic layer (1 unit cell) nonmagnetic $Y_2Ti_2O_7$ spacer layers separating 2, 6, or 10 atomic layer $Y_2V_2O_7$ with a total of 30 atomic layers of $Y_2V_2O_7$ in each film. As a control, we produce submonolayer-shuttered disordered $Y_2Ti_xV_{2-x}O_7$ films with the same Ti:V ratio and overall thickness as each superlattice.

Using a Malvern Panalytical Empyrean four circle diffractometer (Cu Kα_1 radiation, λ = 1.5406 Å) equipped with a Ge(220)x2 monochrometer and Pixcel3D detector, we characterize the structural quality and strain state of our films with x-ray reflectivity (XRR), x-ray diffraction (XRD), and reciprocal space mapping (RSM).

With an Asylum MFP-3d Origin+ atomic force microscope (Oxford Instruments) in tapping mode, we measure sample surface roughness and visualize its topography.

We prepare lamellae for scanning transmission electron microscopy with a Helios 660 focused ion beam system. To verify film structure and superlattice layering, we conduct high-angle annular dark field (HAADF) STEM imaging and electron energy loss spectroscopy (EELS) on a ThermoFisher Scientific Themis Z STEM operating at

200 kV with a convergence angle of 18.9 mrad and collection angle range of 64-200 mrad. Low-angle annular dark field imaging (LAADF) with collection angles from 23-128 mrad yield higher substrate-film contrast. For each micrograph, a stack of short exposure scans are cross-correlated and summed to correct for beam instabilities and drift.

We measure the magnetic properties of the films on a Quantum Design Magnetic Property Measurement System 3 at Harvard's Laukien-Purcell Instrumentation Center. For measurements with the magnetic field applied within the plane of the film, samples are mounted on a quartz rod using GE Varnish (Oxford Instruments) within a clear plastic straw. For out of plane fields, the samples are wedged in place in a straw and secured with clear gel capsules. We measure the magnetic background of a $Y_2Ti_2O_7$ substrate annealed in the MBE at growth conditions. Samples are field-cooled in a 2 kOe applied field and susceptibility is measured in a 500 Oe field unless otherwise specified. Susceptibility measurements are corrected for the substrate background and the temperature independent diamagnetism, then normalized by volume to yield units of μ_B/ V atom. Magnetization versus applied field curves are corrected with substrate subtraction and volume normalization. Ferromagnetic critical temperatures are defined as the temperature at the highest rate of change in susceptibility.

X-ray absorption spectroscopy (XAS) carried out at beamline 6.3.1 at the Advanced Light Source confirms the expected oxidation state and local symmetry environment of V^{4+} in the $Y_2V_2O_7$ thin films. Further, we conduct x-ray magnetic circular dichroism measurements under ± 1.4 T magnetic field to verify the ferromagnetic behavior of the vanadium ions.

Further x-ray magnetic circular dichroism measurements were performed at the I10-1 beamline at the Diamond Light Source. Measurements were done on the V-$L_{2,3}$ edge at 20 K at grazing and normal incidences. For measurements at 1.5 T, we measured with both positive and negative circularly polarized light as well as at both positive and negative field. For measurements at 0.02 T, we measured with only positive field so as to probe the same magnetic state with each measurement. Field dependent data was taken at 514.08 eV with background taken at 510 eV. After background subtraction, field dependent data was normalized to the total of the background and on-peak data.

Synchrotron surface x-ray diffraction measurements are performed at the beamline sector 7-ID-C of the Advanced Photon Source, Argonne National Laboratory, using a six-circle Huber diffractometer in Psi-C geometry. The incident x-ray beam is monochromated to 17.5 keV ($\lambda = 0.70846$ Å) using a Si(111) double-crystal monochromator ($\Delta E/E \approx 1 \times 10^{-4}$), and focused to a 30 μm (vertical) $\times$ 50 μm (horizontal) beam spot size using Kirkpatrick–Baez mirrors The total photon flux at the sample is approximately 3×10^{12} photons/s. Specular ($00L$) Bragg rod measurements are collected with an Eiger2 X 500K area detector up to $L = 3.9$ reciprocal lattice units (r.l.u.), with incident and exit angles matched. Raw 2D detector images are corrected for background scattering, geometric factors, and pixel response non-uniformity. Reciprocal lattice vector (L) is converted to total angular deflection (2θ) using $L = (\frac{2c_0}{\lambda})\sin(\frac{2\theta}{2})$ where c_0 is the substrate lattice parameter (10.01 Å for $Y_2Ti_2O_7$) and λ is the x-ray wavelength (0.70846 Å).

Electronic transport measurements were conducted in a Physical Property Measurement System (Quantum Design) with a Dynacool closed-loop helium compression system.

ACKNOWLEDGMENTS

The authors acknowledge useful conversations with Johanna Nordlander. This work was supported by the Air Force Research Laboratory, Project Grant FA95502110429. J.A.M. acknowledges support from the Packard Foundation and the Gordon and Betty Moore Foundation's EPiQS Initiative, grant GBMF6760. D.F.S. acknowledges support from the NSF Graduate Research Fellowship No. DE-SC0021925. This research used resources of the Advanced Light Source, which is a DOE Office of Science User Facility under contract no. DE-AC02-05CH11231. Crystal growth work at Johns Hopkins University was supported by the Institute for Quantum Matter, an Energy Frontier Research Center funded by DOE, Office of Science, Basic Energy Sciences under Award No. DE-SC0019331. This research was also performed on APS beam time proposal No. 1009892 from the Advanced Photon Source, a U.S. Department of Energy (DOE) Office of Science user facility operated for the DOE Office of Science by Argonne National Laboratory under Contract No. DE-AC02-06CH11357. Sample preparation with focused ion beam was performed at Harvard University's Center for Nanoscale Systems, a member of the National Nanotechnology Coordinated Infrastructure Network, supported by the NSF under grant no. 2025158. Electron microscopy was performed at MIT.nano's Characterization.nano facility with support from Aubrey Penn. The authors thank D. Cui and A. Lowe at Harvard's Laukien-Purcell Instrumentation Center for their assistance with SQUID magnetometry systems.

[1] Shamoto Si, Nakano T, Nozue Y, Kajitani T. Substitution effects on ferromagnetic Mott insulator $Lu_2V_2O_7$. Journal of Physics and Chemistry of Solids 2002;63(6-8):1047–1050.

[2] Pereiro M, Yudin D, Chico J, Etz C, Eriksson O, Bergman A. Topological excitations in a kagome magnet. Nature communications 2014;5(1):4815.

[3] De A, Prabhakaran D, Nair S. Observation of an interfacial magnon-electron drag in a pyrochlore ferromagnet–heavy metal heterostructure. Physical Review B 2025;111(5):054435.

[4] Onose Y, Ideue T, Katsura H, Shiomi Y, Nagaosa N, Tokura Y. Observation of the magnon Hall effect. Science 2010;329(5989):297–299.

[5] Zhang L, Ren J, Wang JS, Li B. Topological magnon insulator in insulating ferromagnet. Physical Review B 2013;87(14):144101.

[6] Mook A, Henk J, Mertig I. Magnon waveguide with nanoscale confinement constructed from topological magnon insulators. Physical Review B 2015;91(17):174409.

[7] Su Y, Wang X, Wang X. Magnonic Weyl semimetal and chiral anomaly in pyrochlore ferromagnets. Physical Review B 2017;95(22):224403.

[8] Shamoto Si, Tazawa H, Ono Y, Nakano T, Nozue Y, Kajitani T. Light-induced metal–insulator transition in $Lu_2V_2O_7$. Journal of Physics and Chemistry of Solids 2001;62(1-2):325–329.

[9] Ullah N, Ali Z, Khan I, Rehman G, Ahmad I. Structural, mechanical and optoelectronic properties of $Y_2M_2O_7$ (M = Ti, V and Nb) pyrochlores: a first principles study. Journal of Electronic Materials 2017;46:4640–4648.

[10] Xiang H, Kan E, Whangbo MH, Lee C, Wei SH, Gong X. Single-ion anisotropy, Dzyaloshinskii-Moriya interaction, and negative magnetoresistance of the spin-$\frac{1}{2}$ pyrochlore $R_2V_2O_7$. Physical Review B 2011;83(17):174402.

[11] Haghighirad A, Gross C, Assmus W. Powder synthesis and crystal growth of $Y_2V_2O_7$ under high pressure and its physical properties. Journal of crystal growth 2008;310(7-9):2277–2283.

[12] Mook A, Henk J, Mertig I. Magnon Hall effect and topology in kagome lattices: A theoretical investigation. Physical Review B 2014;89(13):134409.

[13] Katsura H, Nagaosa N, Lee PA. Theory of the thermal Hall effect in quantum magnets. Physical review letters 2010;104(6):066403.

[14] Ideue T, Onose Y, Katsura H, Shiomi Y, Ishiwata S, Nagaosa N, et al. Effect of lattice geometry on magnon Hall effect in ferromagnetic insulators. Physical Review B—Condensed Matter and Materials Physics 2012;85(13):134411.

[15] Gardner JS, Gingras MJ, Greedan JE. Magnetic pyrochlore oxides. Reviews of Modern Physics 2010;82(1):53–107.

[16] Biswas AA, Jana Y. Crystal-field, exchange interactions and magnetism in pyrochlore ferromagnet $R_2V_2O_7$ (R^{3+} = Y, Lu). Journal of Magnetism and Magnetic Materials 2013;329:118–124.

[17] Ichikawa H, Kano L, Saitoh M, Miyahara S, Furukawa N, Akimitsu J, et al. Orbital ordering in ferromagnetic $Lu_2V_2O_7$. journal of the physical society of japan 2005;74(3):1020–1025.

[18] Mena M, Perry R, Perring T, Le M, Guerrero S, Storni M, et al. Spin-wave spectrum of the quantum ferromagnet on the pyrochlore lattice $Lu_2V_2O_7$. Physical review letters 2014;113(4):047202.

[19] Riedl K, Guterding D, Jeschke HO, Gingras MJ, Valenti R. Ab initio determination of spin Hamiltonians with anisotropic exchange interactions: The case of the pyrochlore ferromagnet $Lu_2V_2O_7$. Physical Review B 2016;94(1):014410.

[20] Miyahara S, Murakami A, Furukawa N. Orbital ordering induced ferromagnetism in $Lu_2V_2O_7$. Journal of molecular structure 2007;838(1-3):223–226.

[21] Hickey A, Lozano-Gómez D, Gingras MJ. Order-by-disorder without quantum zero-point fluctuations in the pyrochlore Heisenberg ferromagnet with Dzyaloshinskii-Moriya interactions. Physical Review B 2025;111(18):184434.

[22] Haghighirad AA, Ritter F, Assmus W. Crystal growth of $A_2V_2O_7$ (A = Y, Er, and Dy) pyrochlores using high pressure. Crystal Growth and Design 2008;8(6):1961–1965.

[23] Zhou H, Choi E, Souza J, Lu J, Xin Y, Lumata L, et al. Magnetic-polaron-driven magnetoresistance in the pyrochlore $Lu_2V_2O_7$. Physical Review B—Condensed Matter and Materials Physics 2008;77(2):020411.

[24] Schlom DG, Chen LQ, Pan X, Schmehl A, Zurbuchen MA. A thin film approach to engineering functionality into oxides. Journal of the American Ceramic Society 2008;91(8):2429–2454.

[25] Nordlander J, Anderson MA, Brooks CM, Holtz ME, Mundy JA. Epitaxy of hexagonal ABO_3 quantum materials. Applied Physics Reviews 2022;9(3).

[26] Jyothis V, Patra B, Chandra VR. Magnon bands in pyrochlore slabs with Heisenberg exchange and anisotropies. Journal of Physics: Condensed Matter 2024;36(18):185801.

[27] Chakhalian J, Liu X, Fiete GA. Strongly correlated and topological states in [111] grown transition metal oxide thin films and heterostructures. APL materials 2020;8(5).

[28] Anderson MA, El Baggari I, Brooks CM, Powell T, Lygouras C, N'Diaye AT, et al. Defect Engineering in Epitaxial Thin Films of the Pyrochlore Frustrated Magnet $Tb_2Ti_2O_7$. Chemistry of Materials 2024;36(5):2325–2333.

[29] Cui Z, Grutter AJ, Zhou H, Cao H, Dong Y, Gilbert DA, et al. Correlation-driven eightfold magnetic anisotropy in a two-dimensional oxide monolayer. Science Advances 2020;6(15):eaay0114. https://www.science.org/doi/abs/10.1126/sciadv.aay0114.

[30] Liu J, Kareev M, Meyers D, Gray B, Ryan P, Freeland JW, et al. Metal-Insulator Transition and Orbital Reconstruction in Mott-Type Quantum Wells Made of $NdNiO_3$. Phys Rev Lett 2012 Sep;109:107402. https://link.aps.org/doi/10.1103/PhysRevLett.109.107402.

[31] Vaz C, Bland J, Lauhoff G. Magnetism in ultrathin film structures. Reports on Progress in Physics 2008;71(5):056501.

[32] Knoke G, Niazi A, Hill J, Johnston D. Synthesis, structure, and ferromagnetism of the oxygen defect pyrochlore system $Lu_2V_2O_{7-x}$ (x= 0.40–0.65). Physical Review B—Condensed Matter and Materials Physics 2007;76(5):054439.

[33] Ristau R, Barmak K, Lewis L, Coffey K, Howard J. On the relationship of high coercivity and L1 ordered phase in CoPt and FePt thin films. Journal of applied physics 1999;86(8):4527–4533.

[34] O'Brien W, Tonner B. Anomalous perpendicular magnetism in Ni/Cu (001) films and the effects of capping layers. Journal of applied physics 1996;79(8):5623–5625.

[35] Su N, Li F, Jiao Y, Liu Z, Sun J, Wang B, et al. Asymmetric ferromagnetic criticality in pyrochlore ferromagnet $Lu_2V_2O_7$. Science Bulletin 2019;64(17):1222–1227.
[36] Spaldin NA. Magnetic materials: fundamentals and applications. Cambridge university press; 2010.

SUPPLEMENTAL MATERIALS: THE EVOLUTION OF MAGNETISM IN A THIN FILM PYROCHLORE FERROMAGNETIC INSULATOR

Margaret A. Anderson†, Megan E. Goh†, Yang Zhang, Kyeong-Yoon Baek, Michael Schulze, Mario Brützam, Christoph Liebald, Chris Lygouras, Dan Ferenc Segedin, Aaron M. Day, Zubia Hasan, Donald A. Walko, Hua Zhou, Peter Bencok, Alpha T. N'Diaye, Charles M. Brooks, Ismail El Baggari, John T. Heron, S. M. Koopayeh, Daniel Rytz, Christo Guguschev, and Julia A. Mundy*

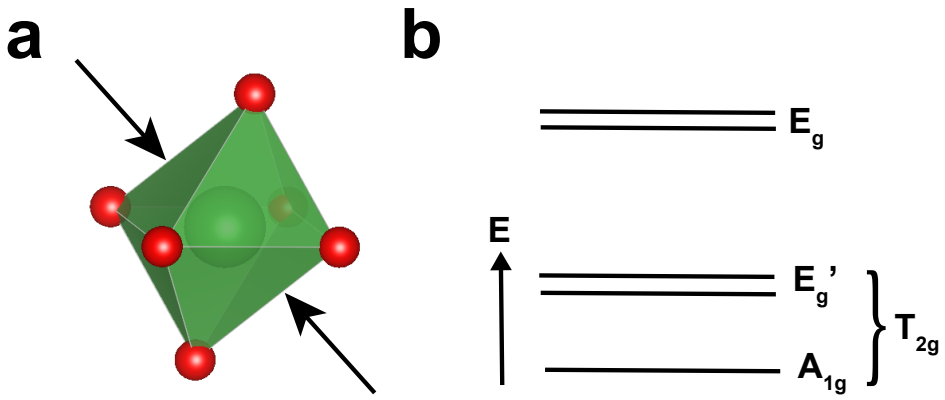


FIG. S1. Oxygen coordination and crystal field levels in $Y_2V_2O_7$. **a** The local oxygen coordination environment of V^{4+} in $Y_2V_2O_7$, which is nearly octahedral with a slight trigonal distortion (emphasized with arrows) **b** The crystal electric field energy levels of V^{4+} with configuration $3d^1$ where the five $3d$ orbitals are split into two degenerate upper E_g levels and three lower energy T_{2g} levels by the octahedral coordination; the three T_{2g} states further split into one lowest lying A_{1g} state and two higher energy E_g' levels due to the trigonal distortion

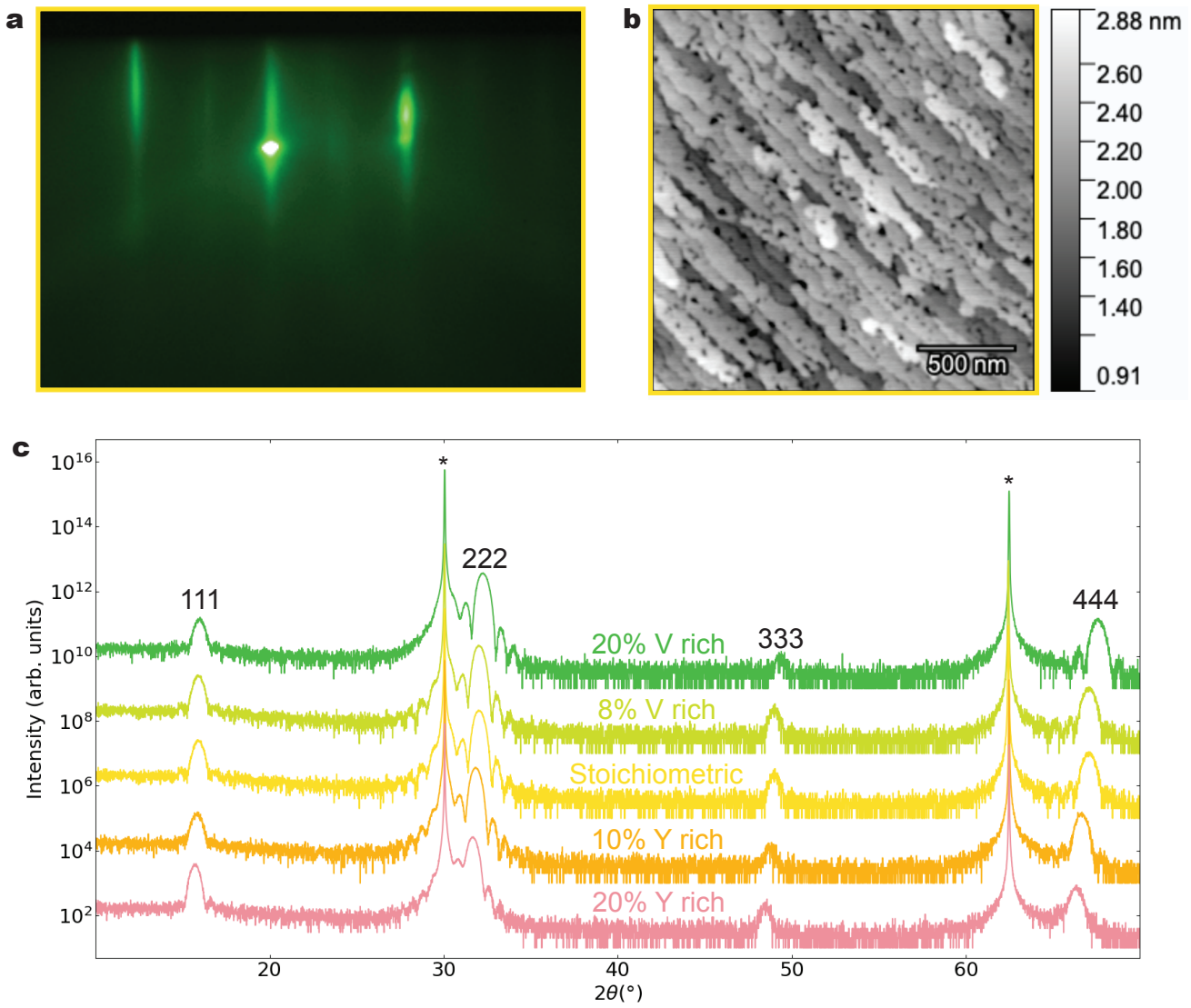


FIG. S2. Structural characterization of YVO_x on YSZ(111). **a** Reflection high energy electron diffraction (RHEED) of YVO_x on YSZ(111) **b** Atomic force microscopy of a film showing a smooth surface with an RMS roughness of 322 pm **c** X-ray diffraction of YVO_x on YSZ(111) with varying stoichiometry. Asterisks indicate substrate diffraction peaks and lattice plane indices denote film peaks.

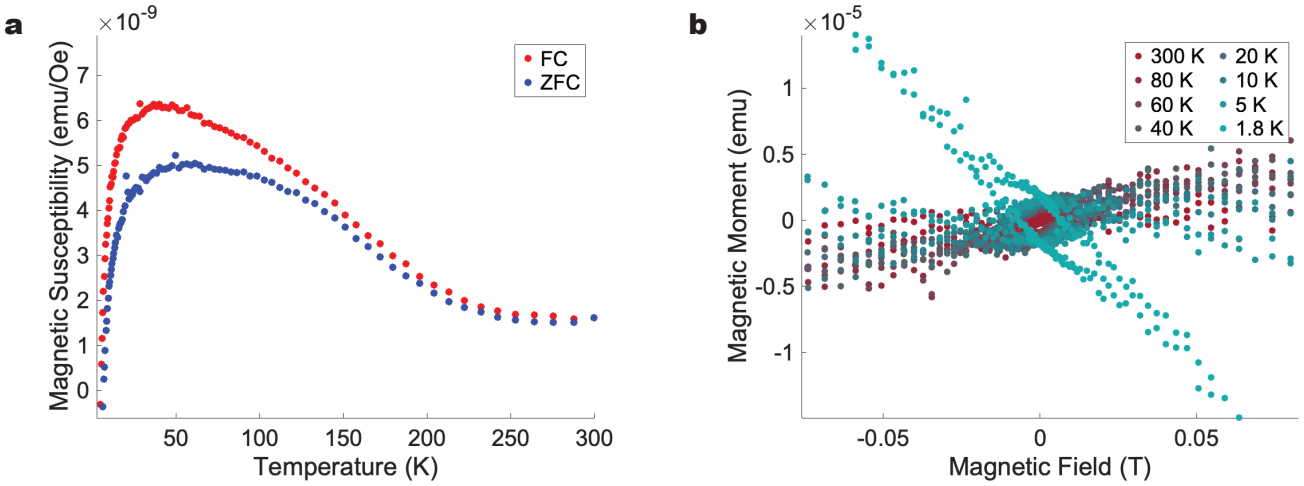


FIG. S3. Magnetic characterization of YVO_x on YSZ(111). **a** Field-cooled vs. zero-field-cooled (ZFC) magnetic susceptibility of stoichiometric film **b** Magnetization vs. in-plane applied field loops for stoichiometric YVO_x on YSZ(111)

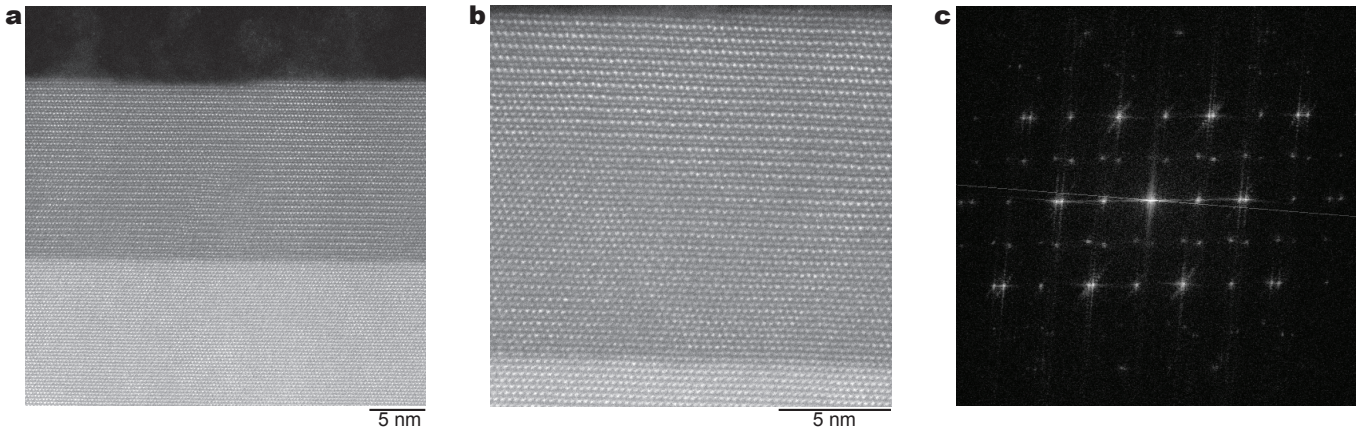


FIG. S4. STEM imaging of YVO_x on YSZ(111). **a** a large field-of-view HAADF-STEM micrograph along YSZ $\langle 1\bar{1}0 \rangle$ **b** a higher magnification image of the film in (a) showing the lack of in-plane pyrochlore order in the film **c** a fast Fourier transform (FFT) of the YVO_x film showing doubled intermediate peaks reminiscent of the pyrochlore-like defect fluorite structure, but with out-of-plane pyrochlore order

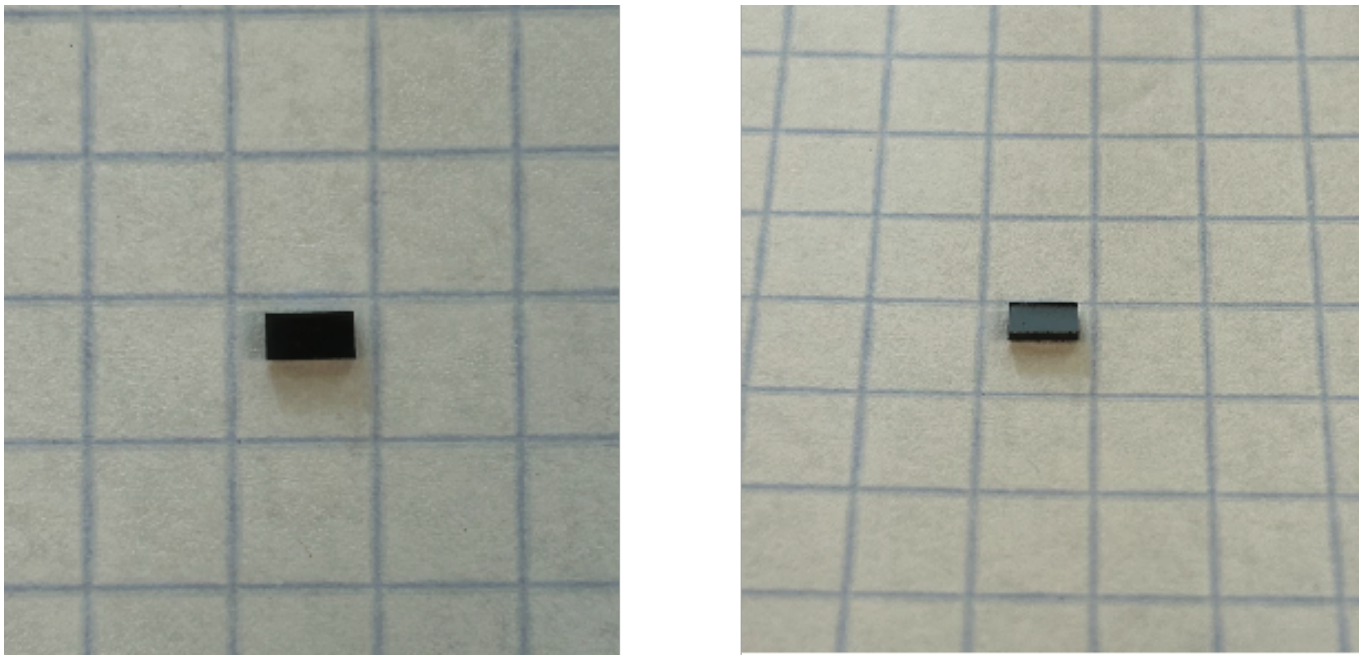


FIG. S5. Images of noncommercial $Y_2Ti_2O_7$ substrates. A top down view where each box is 5mm x 5mm (left); An angled view to show the smooth polished surface (right)

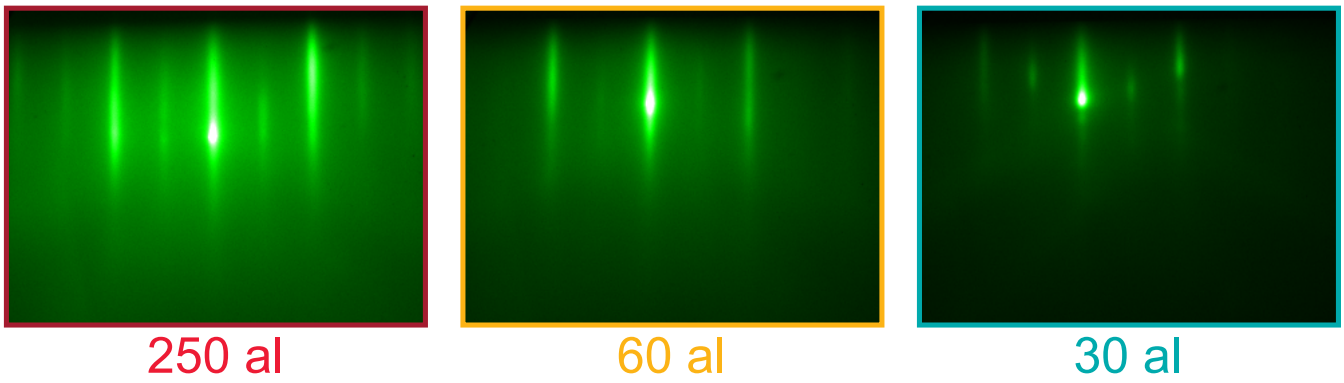


FIG. S6. Reflection high energy electron diffraction (RHEED) patterns after deposition for selected films in the $Y_2V_2O_7$ thickness series on $Y_2Ti_2O_7$.

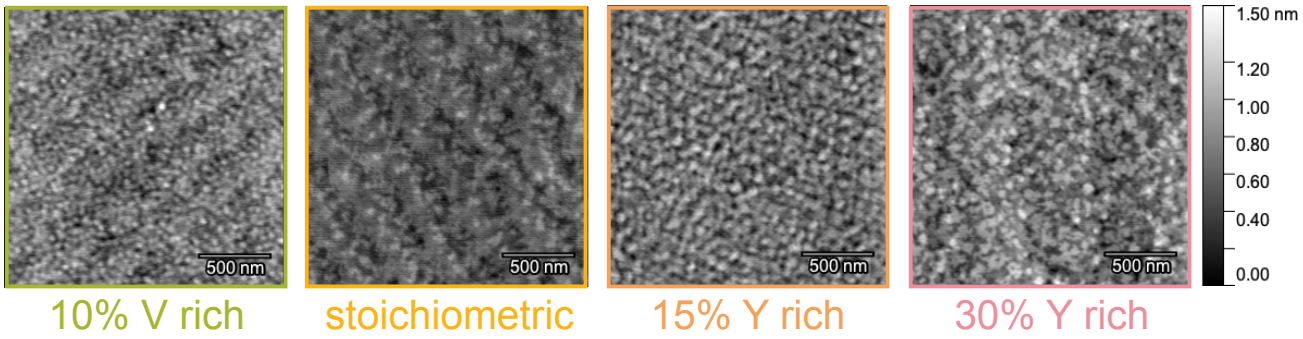


FIG. S7. Surface topography of $Y_2V_2O_7$ on $Y_2Ti_2O_7$ with varying stoichiometry. Atomic force microscopy shows smooth surfaces with a texture that depends on stoichiometry; RMS surface roughness values are 176.8 pm for the 10% V rich film, 142.3 pm for the stoichiometric film, 190.8 pm for the 15% Y rich film, and 208.8 pm for the 30% Y rich film

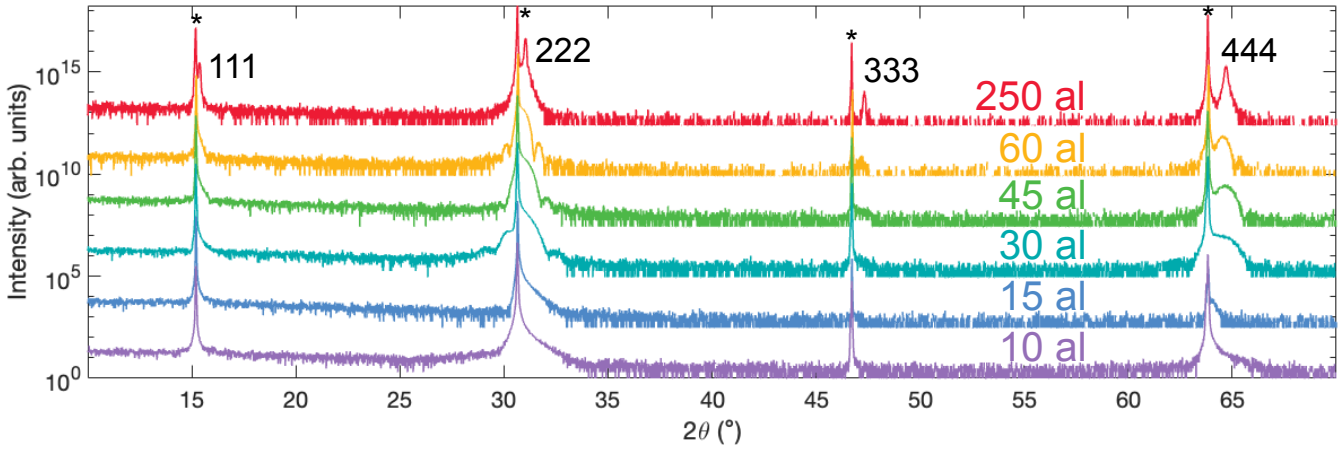


FIG. S8. Complete x-ray diffraction of the stoichiometric $Y_2V_2O_7$ thickness series on $Y_2Ti_2O_7$. Asterisks indicate substrate diffraction peaks and lattice plane indices denote film peaks.

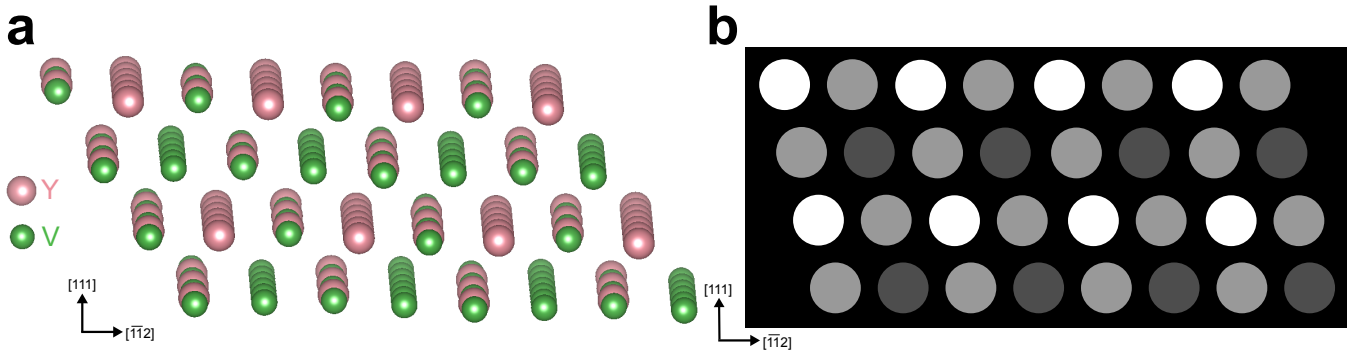


FIG. S9. An ideal pyrochlore in STEM imaging. **a** The cations in $Y_2V_2O_7$ viewed along $\langle 1\bar{1}0\rangle$ and slightly tipped off axis to show the composition of atomic columns; columns are either purely yttrium, purely vanadium, or alternating yttrium and vanadium out-of-plane **b** A schematic of the ideal pyrochlore structure along $\langle 1\bar{1}0\rangle$ in STEM where the apparent brightness of atomic columns scales with atomic number Z; alternating light and dark rows and slanted columns form a checkerboard pattern where the brightest quarter of spots are pure yttrium columns, the darkest quarter are pure vanadium columns, and half of the spots have an intermediate brightness corresponding to the mix of yttrium and vanadium

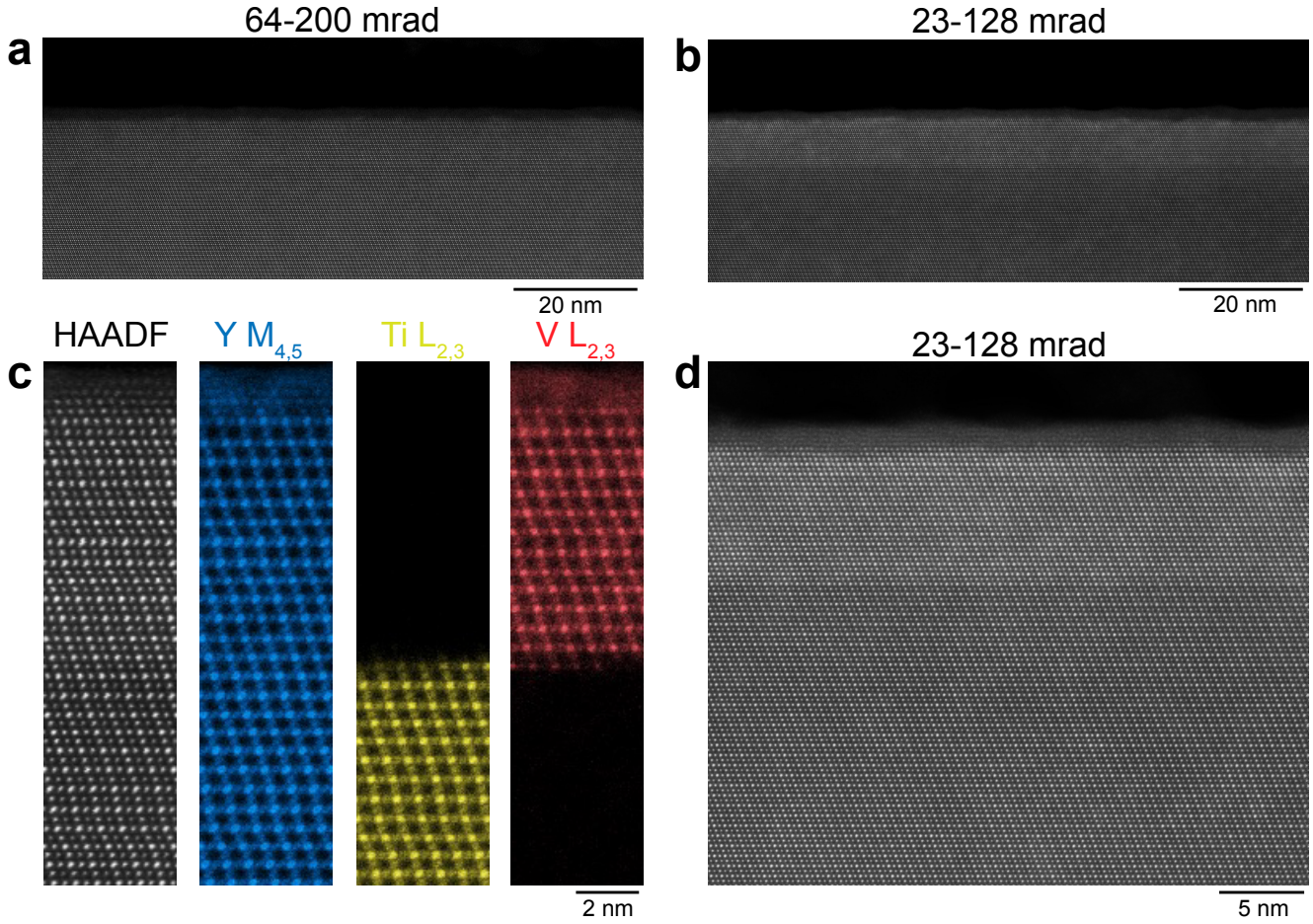


FIG. S10. Additional STEM-EELS imaging on $Y_2V_2O_7$ on $Y_2Ti_2O_7$. **a** A large field of view HAADF-STEM image with the same conditions as Figure 1c with collection angle range 64-200 mrad **b** A large field of view LAADF-STEM image with collection angle 23-128 mra, which emphasizes the substrate-film interface **c** From left to right: a HAADF-STEM micrograph of the region of interest, a concentration map of yttrium, a map of titanium concentration, and a vanadium concentration map of the same region as Figure 1d **d** A higher magnification view of (b)

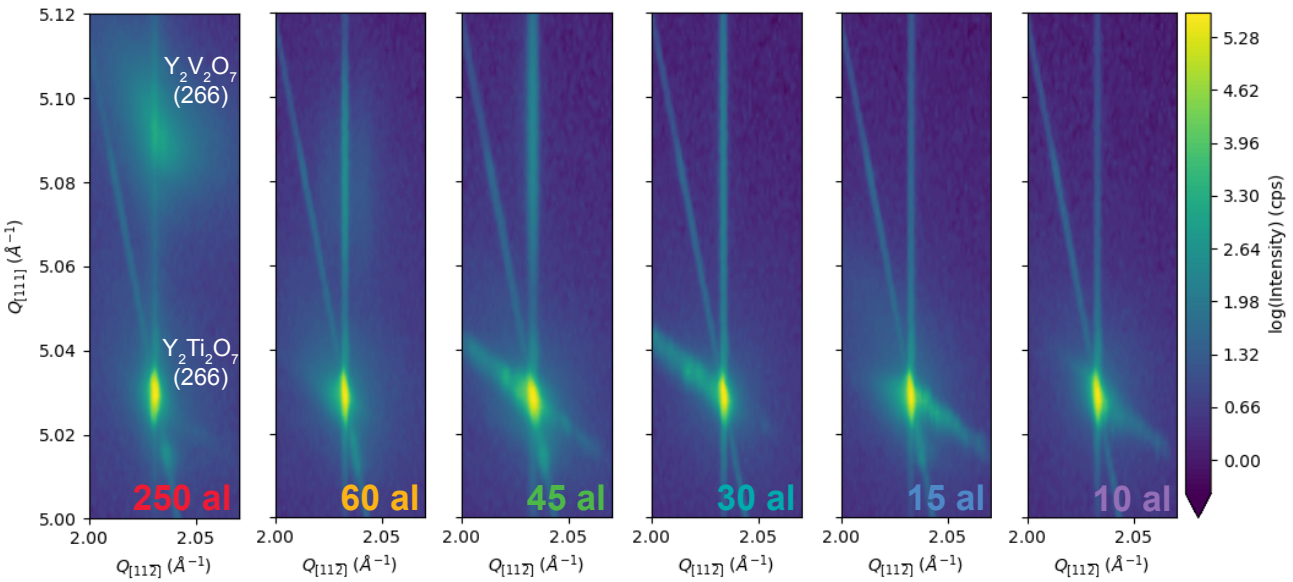


FIG. S11. Reciprocal space mapping of $Y_2V_2O_7$ thin films. The appearance of a diffuse background around the film peak for films with thickness above 45 atomic layers indicates partial strain relaxation.

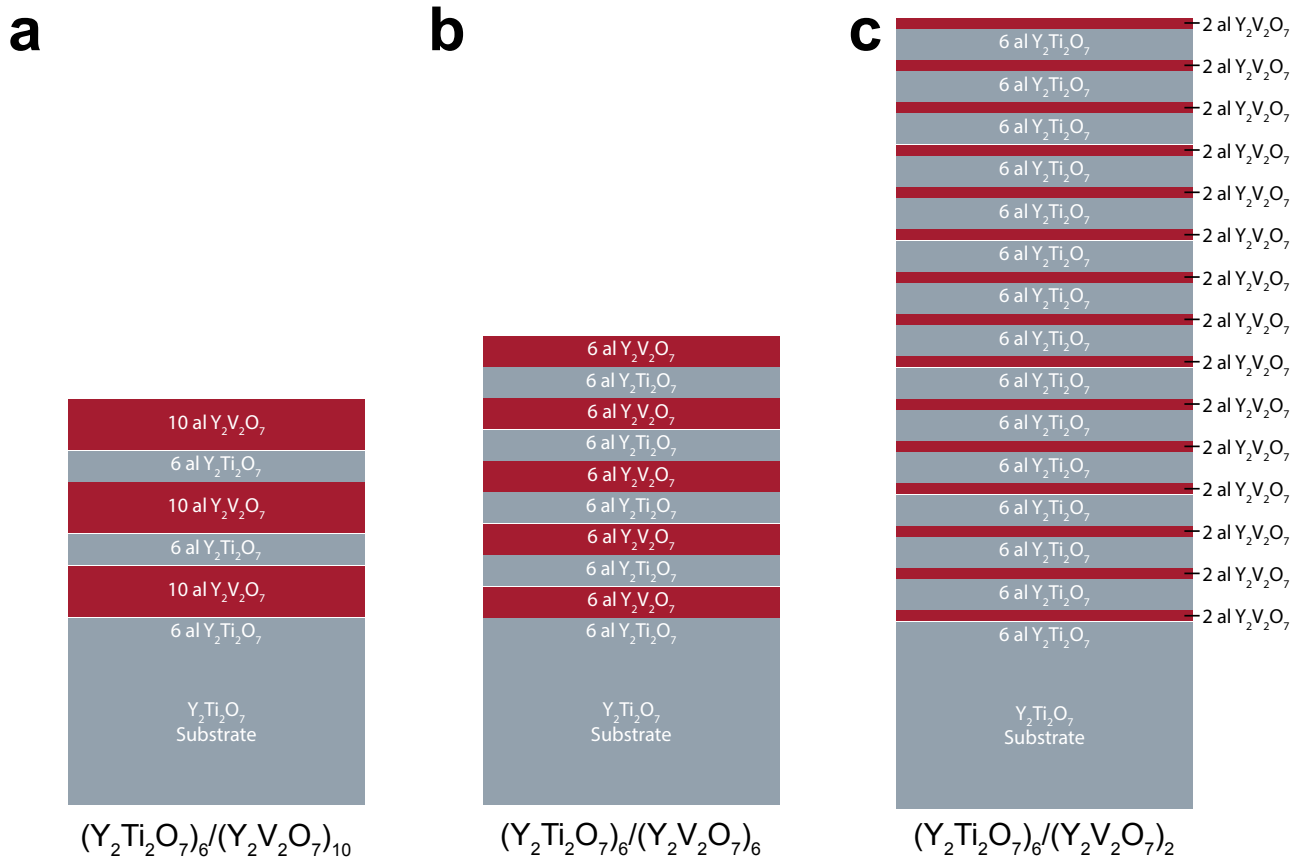


FIG. S12. Schematic of $(Y_2Ti_2O_7)_m/(Y_2V_2O_7)_n$ superlattices **a** The layering scheme for the $(Y_2Ti_2O_7)_6/(Y_2V_2O_7)_{10}$ superlattice with 3 repeats to yield a total of 30 atomic layers of $Y_2V_2O_7$ **b** The layering scheme for the $(Y_2Ti_2O_7)_6/(Y_2V_2O_7)_6$ superlattice with 5 repeats giving 30 total atomic layers of $Y_2V_2O_7$ **c** The layering scheme for the $(Y_2Ti_2O_7)_6/(Y_2V_2O_7)_2$ superlattice with 15 repeats to yield 30 total atomic layers of $Y_2V_2O_7$

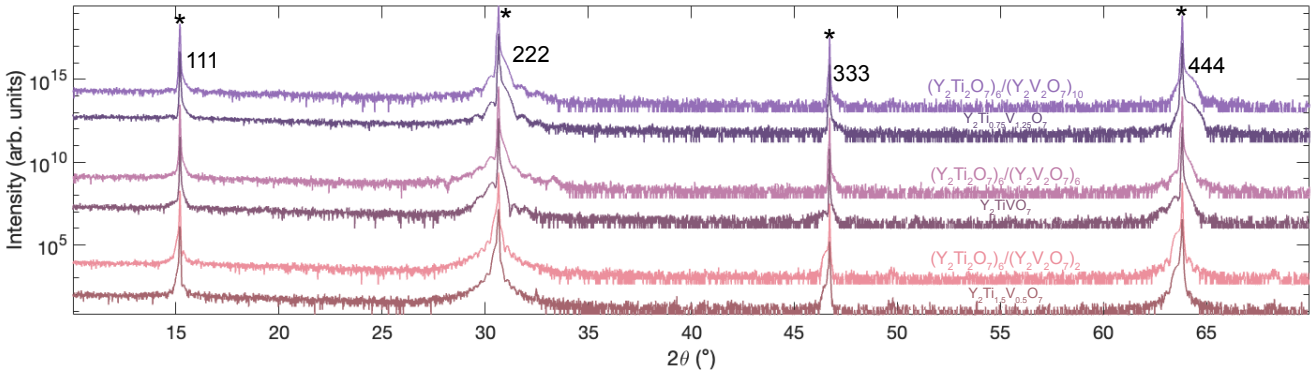


FIG. S13. X-ray diffraction of $(Y_2Ti_2O_7)_m/(Y_2V_2O_7)_n$ superlattices and their disordered counterparts. $Y_2Ti_2O_7$ substrate peaks indicated by asterisk; film peaks denoted by plane indices. Each pair of scans gives the ordered superlattice (top) corresponding to the schematics in Figure S12 and a corresponding solid solution (bottom) with the same composition and total thickness. A possible superlattice peak exists at $2\theta = 33^\circ$ within the $(Y_2Ti_2O_7)_6/(Y_2V_2O_7)_6$ superlattice, not seen within the corresponding disordered film Y_2TiVO_7.

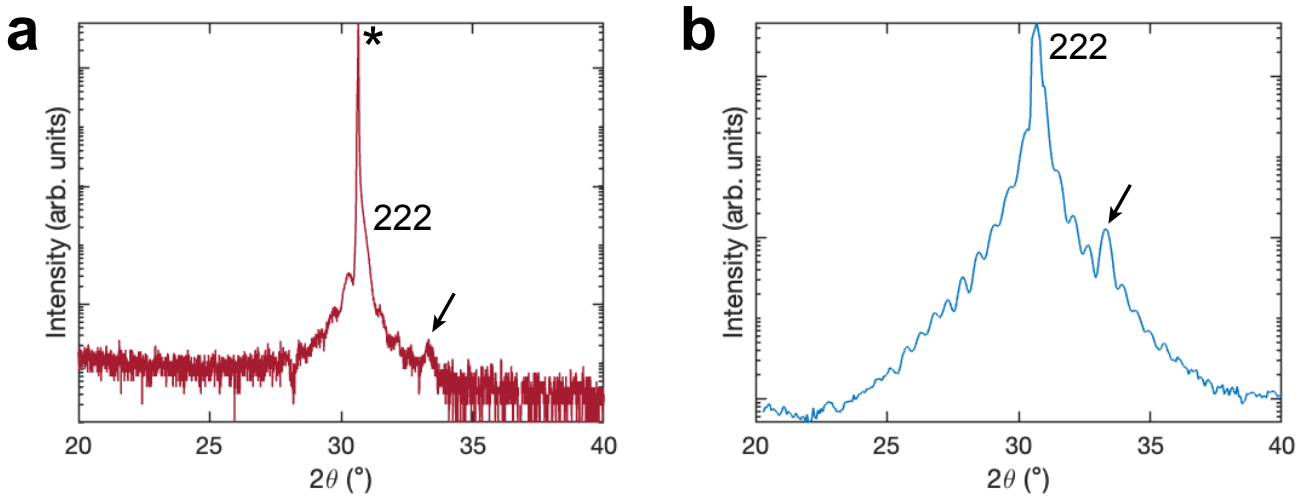


FIG. S14. X-ray diffraction of a $(Y_2Ti_2O_7)_6/(Y_2V_2O_7)_6$ superlattice. **a** X-ray diffraction of $(Y_2Ti_2O_7)_6/(Y_2V_2O_7)_6$ using a Malvern Panalytical Empyrean Cu Kα diffractometer, which shows the 222 film peak adjacent to the 222 $Y_2Ti_2O_7$ substrate peak (indicated with an asterisk) with a possible weak superlattice peak (indicated by an arrow) **b** synchrotron x-ray diffraction data of the same sample as in (a) with the substrate subtracted showing the 222 film peak and a clear superlattice peak (indicated by an arrow)

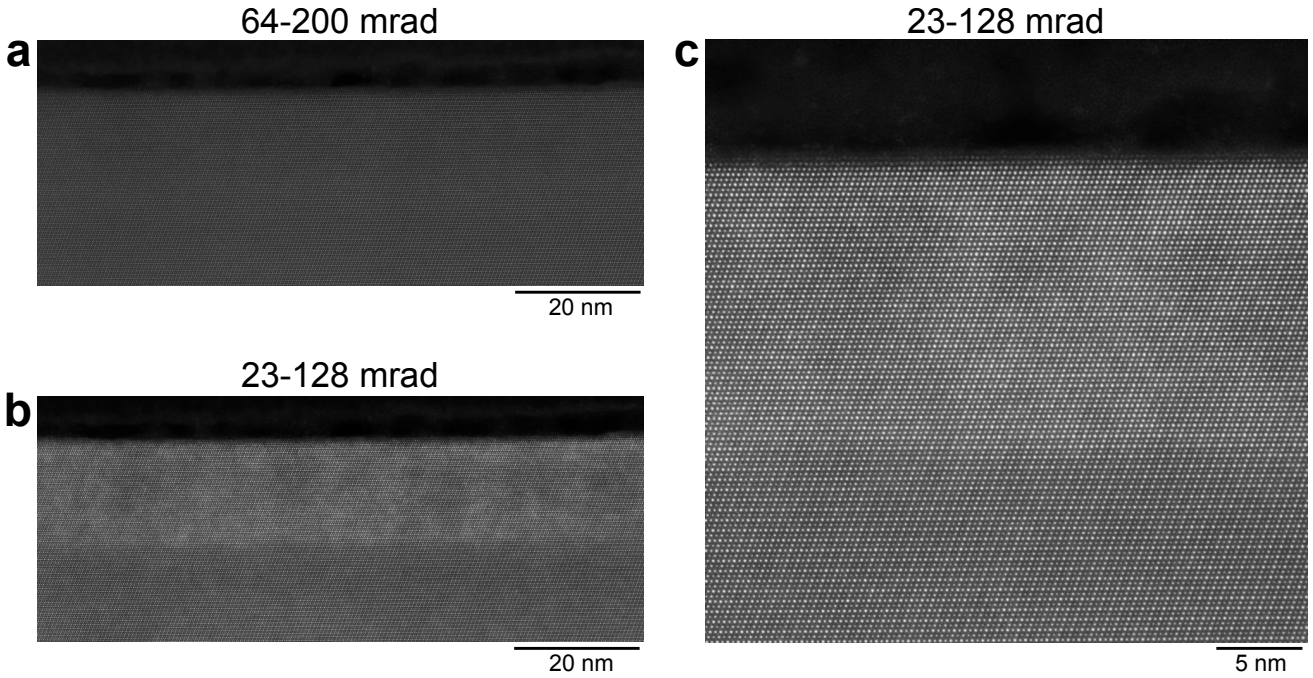


FIG. S15. STEM imaging of $(Y_2Ti_2O_7)_6/(Y_2V_2O_7)_6$ superlattice on $Y_2Ti_2O_7$. **a** A large field of view HAADF-STEM micrograph with collection angle range 64-200 mrad showing the high structural quality of the film over a large region **b** A large field of view LAADF-STEM image with collection angle 23-128 mrad, which highlights the substrate-film interface **c** A higher magnification view of (b)

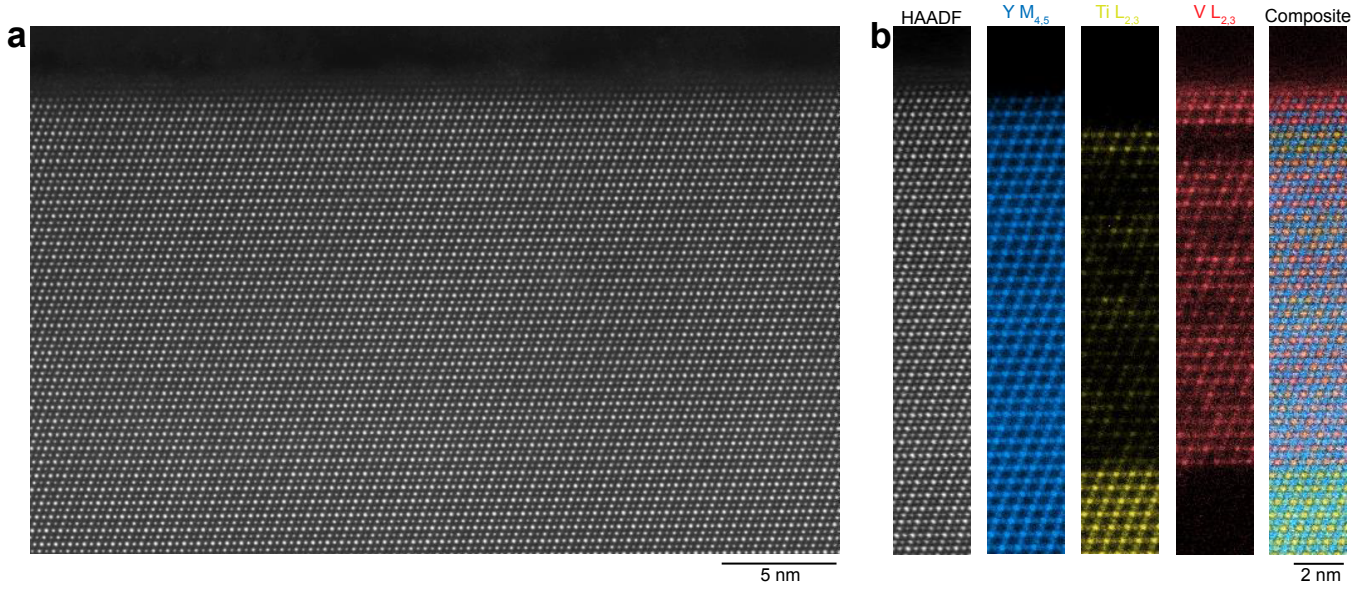


FIG. S16. STEM-EELS imaging of $(Y_2Ti_2O_7)_6/(Y_2V_2O_7)_6$ superlattice on $Y_2Ti_2O_7$. **a** A HAADF-STEM micrograph taken along $\langle 1\bar{1}0\rangle$ with collection angle 64-200 mrad (same conditions as Figure S15a) **b** From left to right: a HAADF-STEM micrograph of the region of interest at approximately the same scale as (a), an EELS concentration map of yttrium, a map of titanium concentration, a vanadium concentration map, and a composite view showing the layering within the superlattice sample. Diffusion increases deeper within the film, disrupting the clear 6 monolayer repeat visible at the surface of the film.

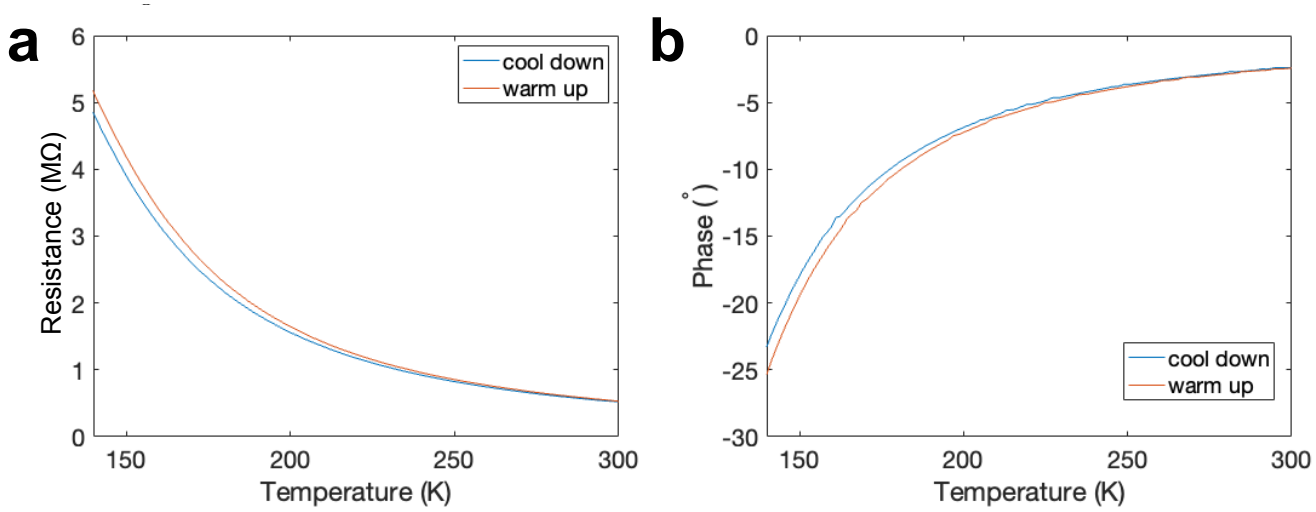


FIG. S17. Insulating transport behavior of a 60 atomic layer $Y_2V_2O_7$ film on $Y_2Ti_2O_7$. **a** Insulating behavior where resistance increases rapidly with decreasing temperature; an Arrenhius fit to the high temperature data estimates the band gap of about 50 meV, below bulk estimates of 0.2-0.33 eV; thinner films exhibit higher surface resistance at room temperature **b** The phase of the resistance measurement increases rapidly with decreasing temperature, which indicates the sample becomes highly resistive and the resistance measurement becomes less reliable

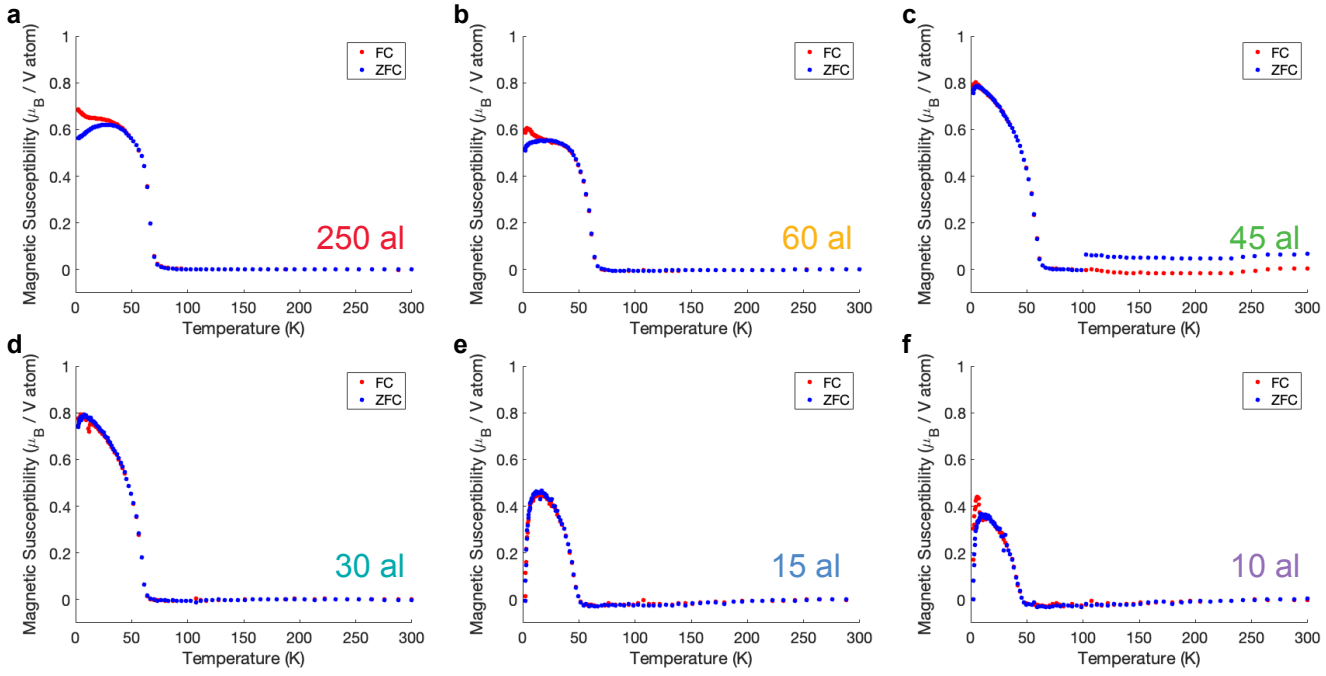


FIG. S18. Field-cooled versus zero-field-cooled (ZFC) magnetic susceptibility of $Y_2V_2O_7$ thickness series. **a-f** The zero-field-cooled (ZFC, blue) and 2 kOe field-cooled (FC, red) magnetic susceptibilities measured in a 500 Oe in-plane applied field for films with thickness (a) 250, (b) 60, (c) 45, (d) 30, (e) 15, and (f) 10 atomic layers of $Y_2V_2O_7$ on isostructural $Y_2Ti_2O_7(111)$. The FC and ZFC curves diverge at low temperatures in the films at or above about 45 atomic layers thick, which suggests hysteresis opens in a changing applied field at these thicknesses and temperatures (as seen in Figure 3)

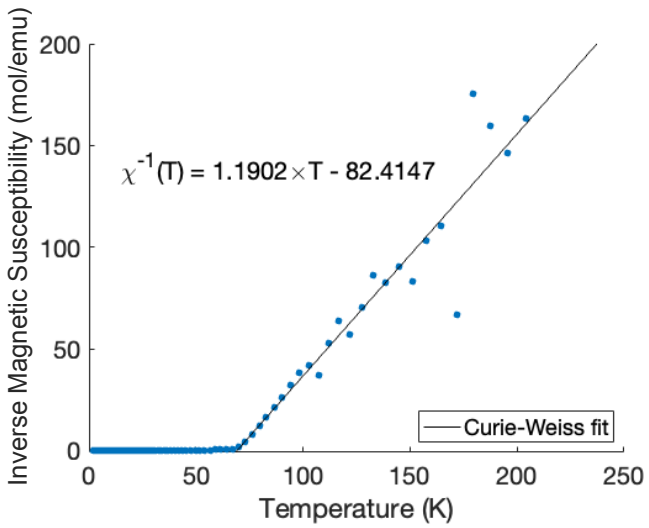


FIG. S19. Curie-Weiss fit of the inverse magnetic susceptibility of 250 atomic layer $Y_2V_2O_7$. A linear fit to the inverse field-cooled susceptibility between 80 and 200 K yields an estimated Curie-Weiss temperature of 69 K and $\mu_{\text{eff}} = 1.83\ \mu_B$/V atom.

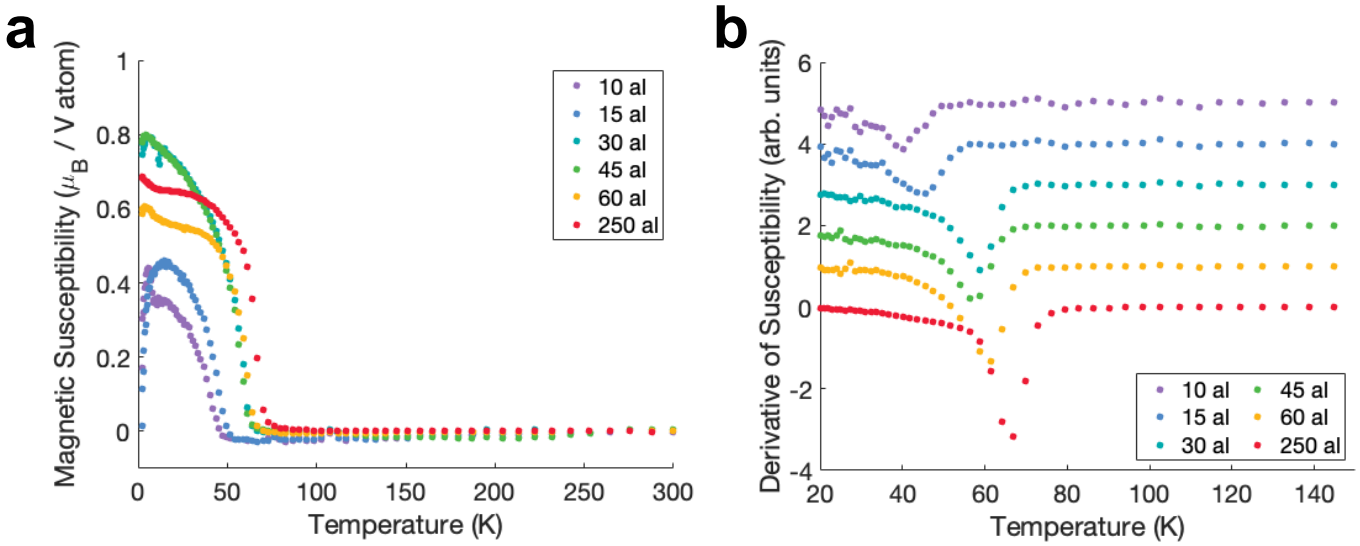


FIG. S20. Volume normalization and derivative of the susceptibility of the $Y_2V_2O_7$ thickness series. **a** The substrate subtracted, diamagnetism corrected, volume normalized, field-cooled magnetic susceptibility of the $Y_2V_2O_7$ measured in a 500 Oe field shifted to align at high temperatures **b** The derivatives of the susceptibilities plotted in (a) with a vertical shift for clarity; T_c is defined as the temperature where the absolute value of the derivative is maximized

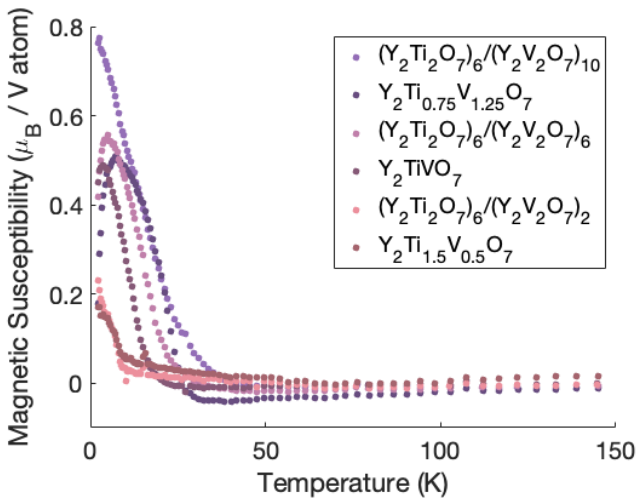


FIG. S21. Magnetic susceptibility of the $(Y_2Ti_2O_7)_6/(Y_2V_2O_7)_n$ superlattices. The substrate subtracted, diamagnetism corrected, volume normalized, field-cooled magnetic susceptibility of the $(Y_2Ti_2O_7)_6/(Y_2V_2O_7)_n$ and corresponding solid solution films on $Y_2Ti_2O_7$ measured in a 500 Oe field shifted to align at high temperatures

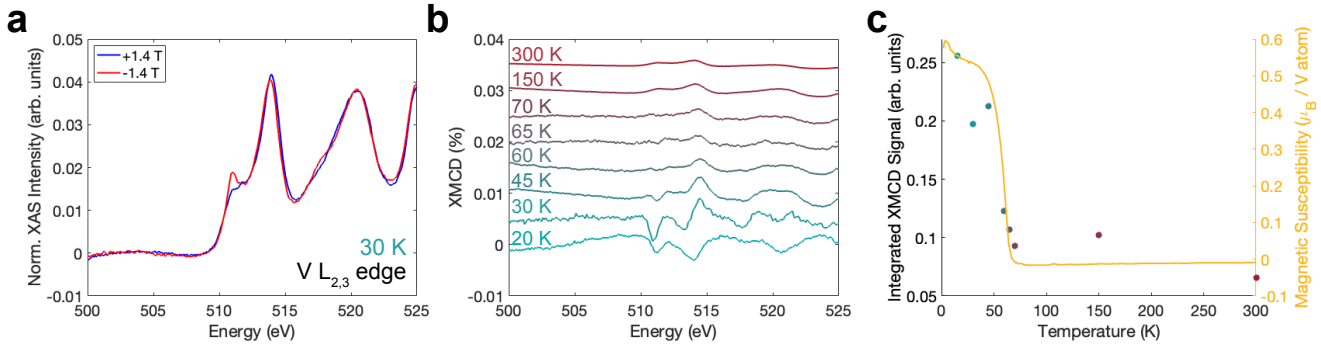


FIG. S22. X-ray circular magnetic dichroism (XMCD) of $Y_2V_2O_7$ on $Y_2Ti_2O_7$. **a** X-ray absorption spectroscopy of the V-$L_{2,3}$ edge of a 60 atomic layer $Y_2V_2O_7$ thin film under grazing incidence σ^+ polarized light at 30 K under $\pm$1.4 T applied field; The XAS spectra show the expected shape for V^{4+} in a nearly octahedral coordination environment **b** The XMCD signal at various temperatures extracted from the difference of XAS signals in $\pm$1.4 T applied fields as in (a) **c** The correspondence between the integrated XMCD signal of the $Y_2V_2O_7$ film at different temperatures and the magnetic susceptibility measured with SQUID magnetometry.

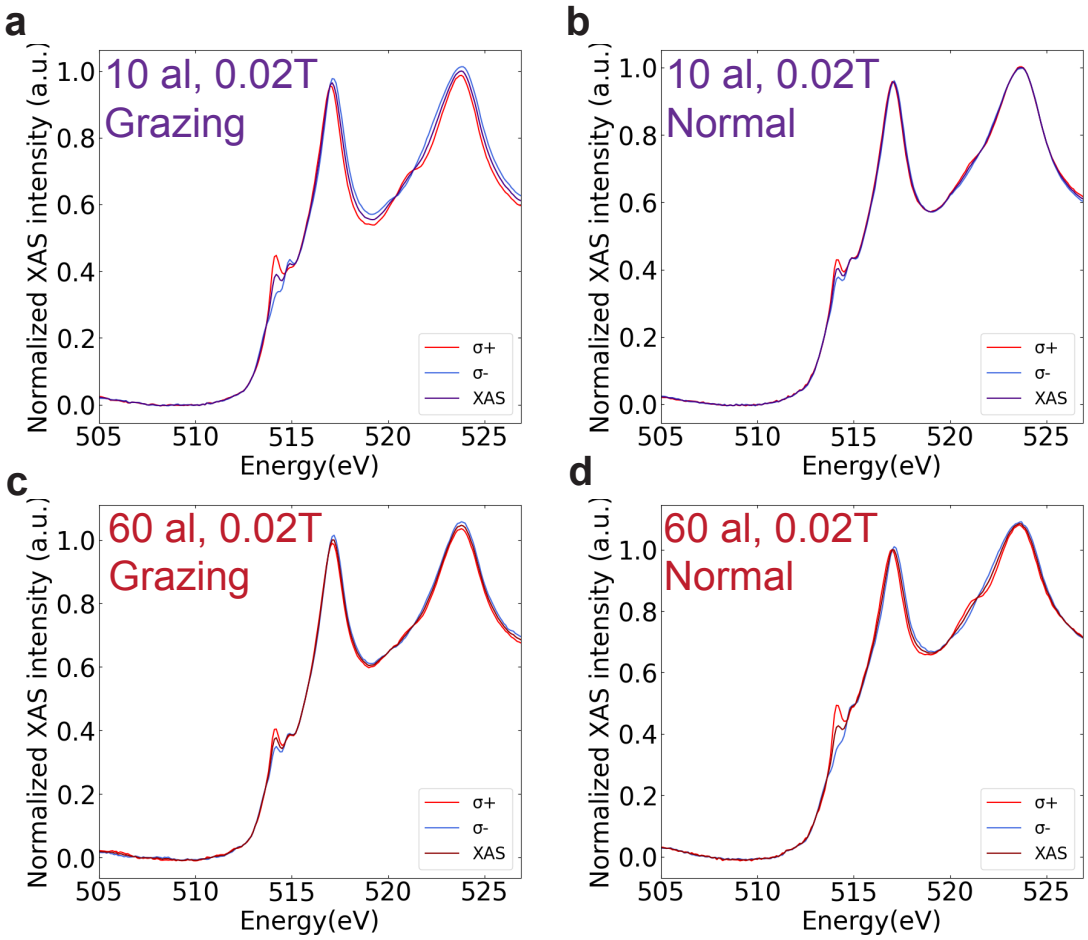


FIG. S23. X-ray absorption spectroscopy (XAS) of $Y_2V_2O_7$ on $Y_2Ti_2O_7$ measured at 20 K and 0.02 T **a, b** XAS of 10 atomic layer sample at grazing and normal incidences **c, d** XAS of 10 atomic layer sample at grazing and normal incidences

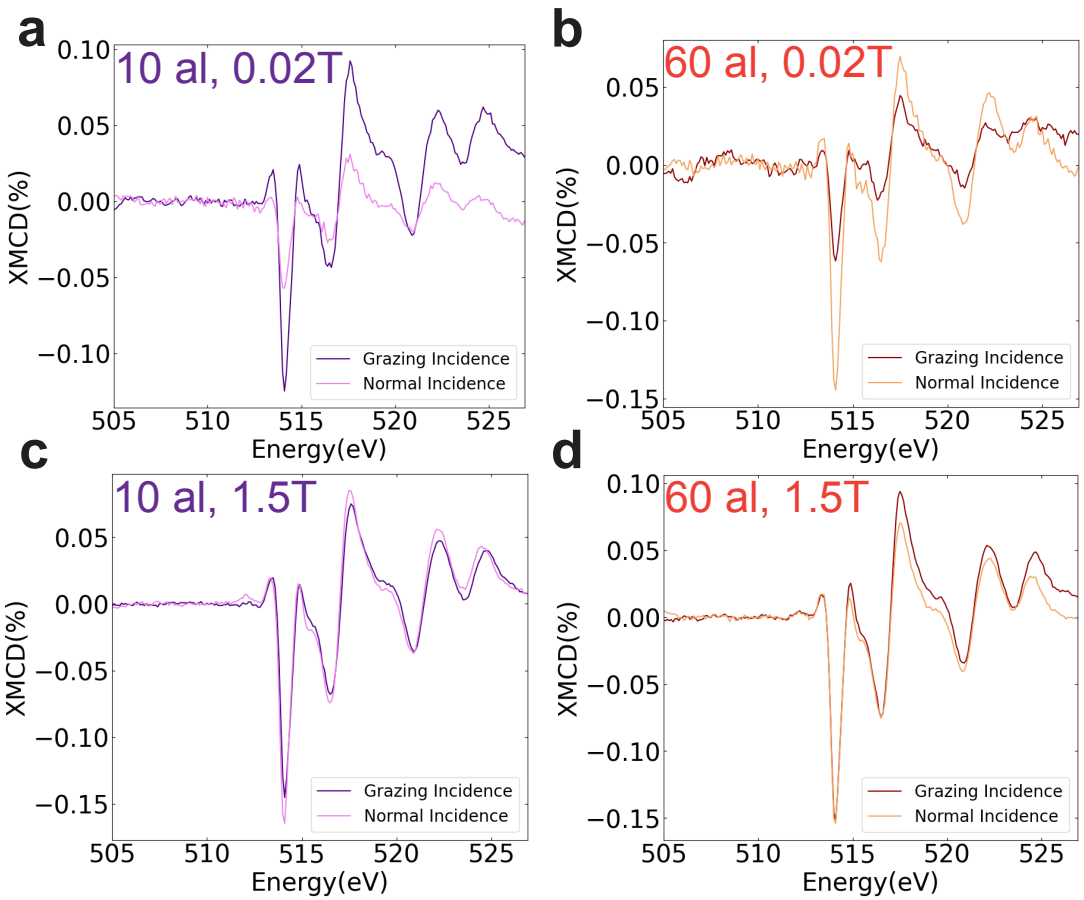


FIG. S24. Angle Dependent XMCD of $Y_2V_2O_7$ on $Y_2Ti_2O_7$ measured at 20 K. **a, b** XMCD signal at the V-$L_{2,3}$ edge of 10 atomic layer and 60 atomic layer films at 0.02 T measured at both normal (90°) and grazing (20°) incidences; a change in anisotropy is observed as stronger XMCD signal switches from grazing incidence in the 10 atomic layer film to normal incidence in the 60 atomic layer film **c, d** XMCD signal at the V-$L_{2,3}$ edge of 10 atomic layer and 60 atomic layer films at 1.5 T measured at both normal (90°) and grazing (20°) incidences; after saturation of the magnetic moments in the 1.5 T applied field, anisotropy is no longer clearly observed

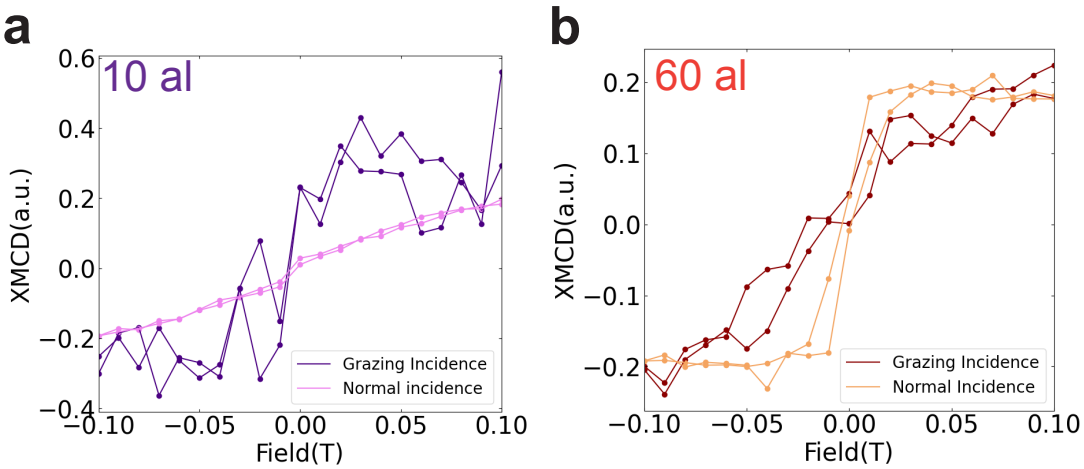


FIG. S25. Field dependent XMCD of $Y_2V_2O_7$ at 514.08 eV, where we observed the largest XMCD signal within the V-$L_{2,3}$ edge. Background scans were taken at 510 eV and subtracted from on-peak data **a** Field dependence from -0.1 to 0.1 T of 10 atomic layer film at grazing and normal incidence; we observe the grazing incidence reaches saturation at lower field **b** Field dependence from -0.1 to 0.1 T of 60 atomic layer film at grazing and normal incidence; we observe the normal incidence reaches saturation at lower field

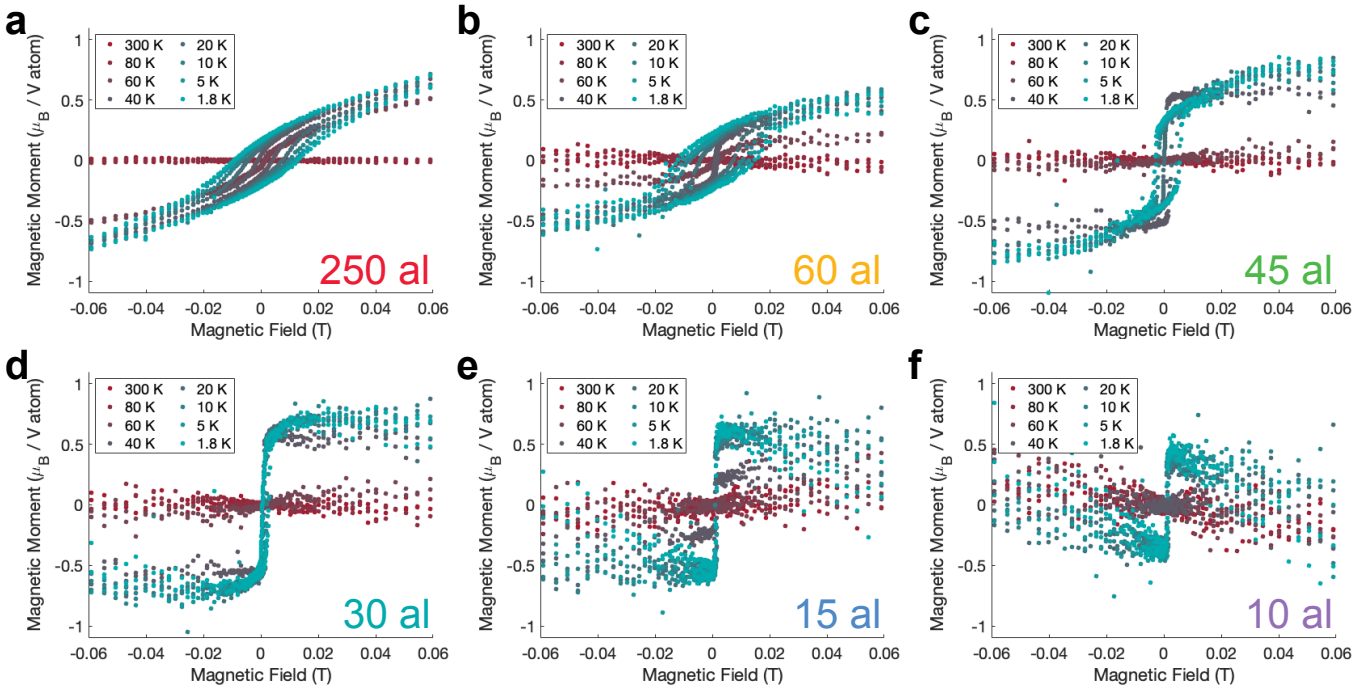


FIG. S26. Magnetization vs. in-plane applied field loops for $Y_2V_2O_7$ thickness series. **a-f** Temperature dependence of magnetization vs. applied field with field perpendicular to ⟨111⟩ (in-plane) for (a) 250, (b) 60, (c) 45, (d) 30, (e) 15, and (f) 10 atomic layers of $Y_2V_2O_7$ on $Y_2Ti_2O_7$; (b) is identical to Figure 3b in the main text

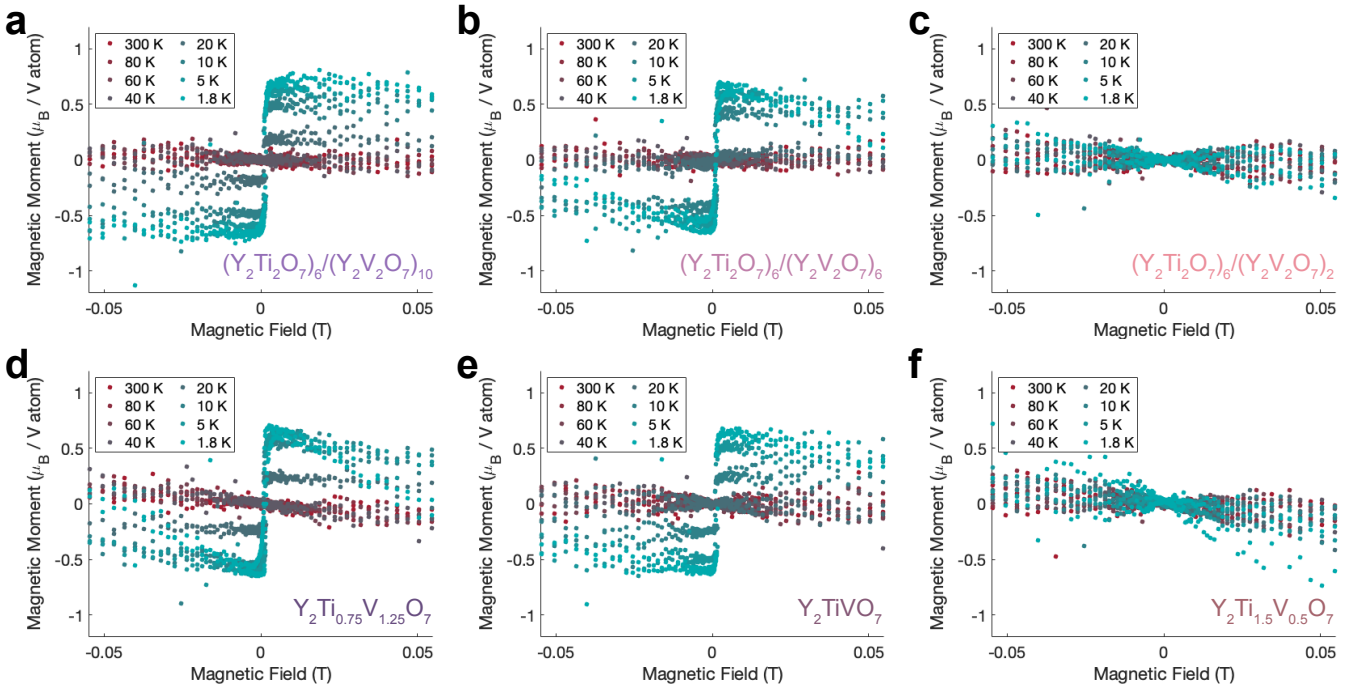


FIG. S27. Magnetization vs. in-plane applied field loops for $(Y_2Ti_2O_7)_6/(Y_2V_2O_7)_n$ superlattices. **a-f** Temperature dependence of magnetization vs. applied field with field perpendicular to ⟨111⟩ (in-plane) for (a) $n = 10$ and (d) corresponding cation disordered film $Y_2Ti_{0.75}V_{1.25}O_7$, (b) $n = 6$ and (e) corresponding Y_2TiVO_7, and (c) $n = 2$ and (f) corresponding $Y_2Ti_{1.5}V_{0.5}O_7$ on $Y_2Ti_2O_7$

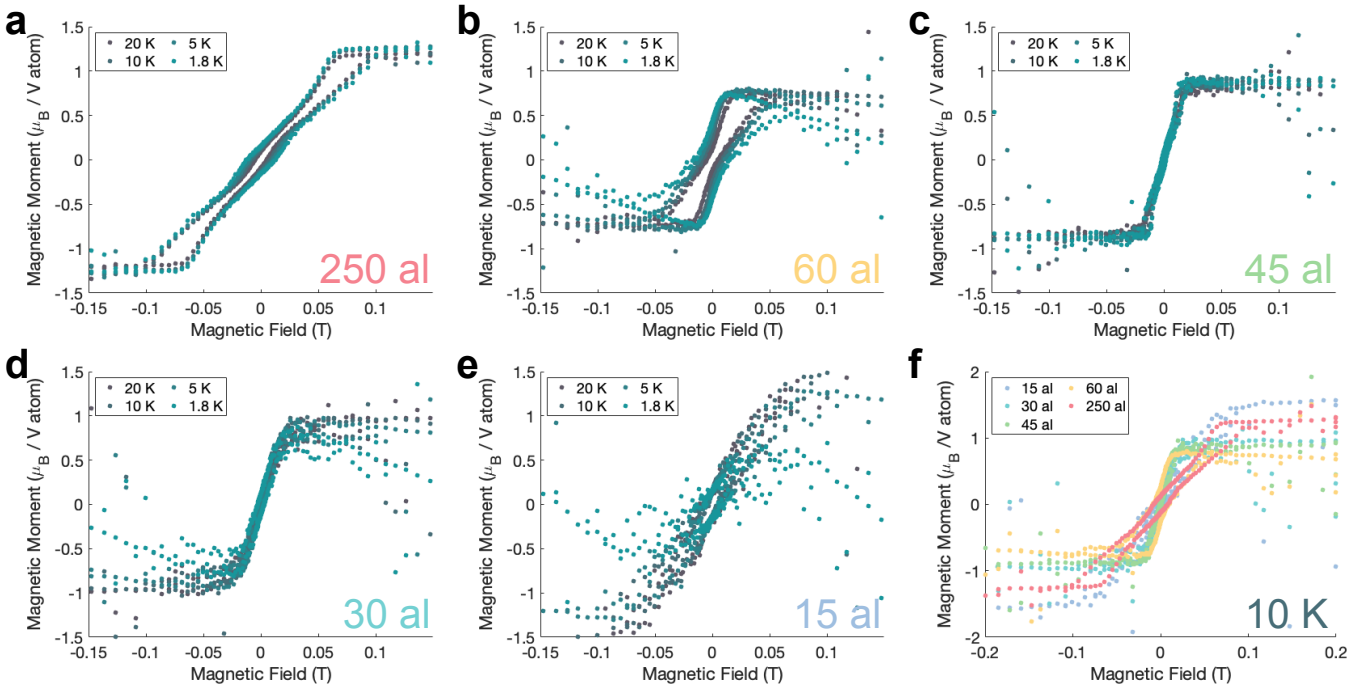


FIG. S28. Magnetization vs. out-of-plane applied field loops for $Y_2V_2O_7$ thickness series. **a-e** Temperature dependence of magnetization vs. applied field with field along ⟨111⟩ (out-of-plane) for (a) 250, (b) 60, (c) 45, (d) 30, and (e) 15 atomic layers of $Y_2V_2O_7$ on $Y_2Ti_2O_7$ **f** Thickness dependence of magnetization vs. applied field loops measured at 10 K with field along ⟨111⟩

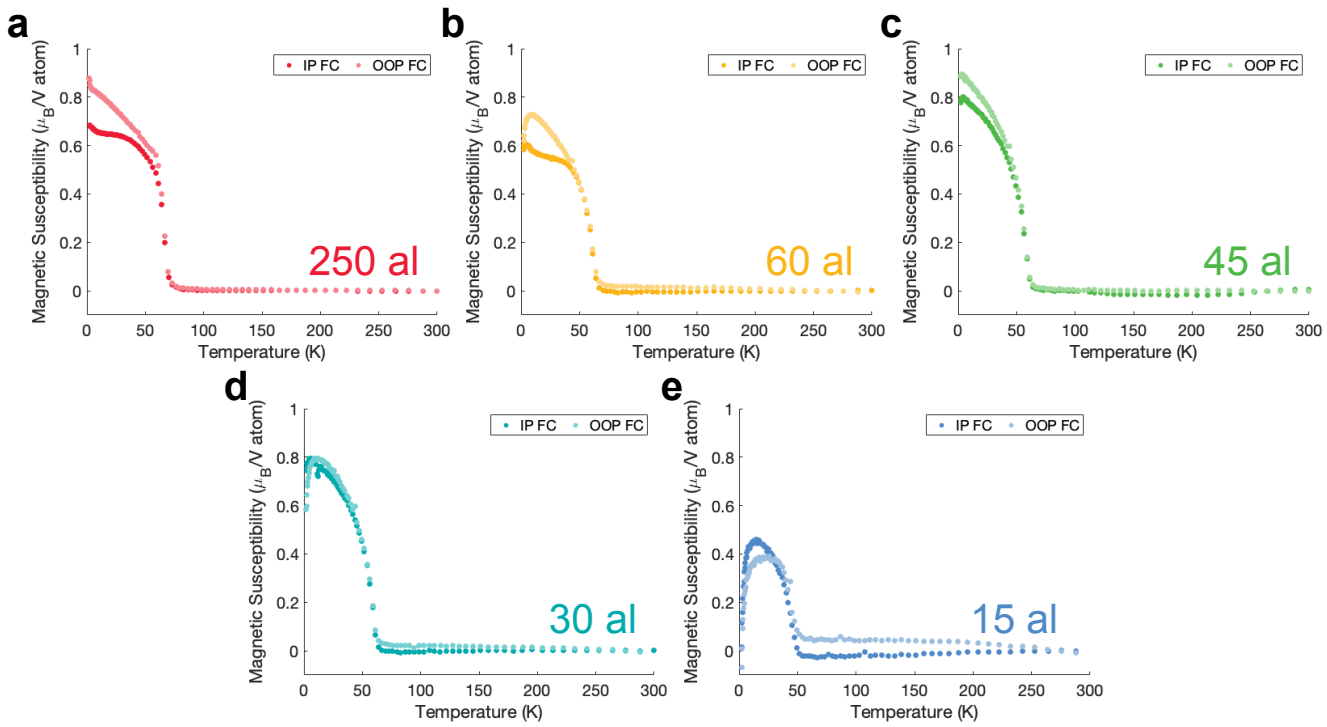


FIG. S29. Anisotropy of the magnetic susceptibility of $Y_2V_2O_7$ thickness series. **a-e** Magnetic susceptibility vs. temperature for a field applied within the plane of the film (IP, perpendicular to ⟨111⟩) and out-of-plane (OOP, along ⟨111⟩) for films with thickness (a) 250, (b) 60, (c) 45, (d) 30, and (e) 15 atomic layers, which show the same anisotropy trend as the magnetization vs. applied field loops in Figure 4

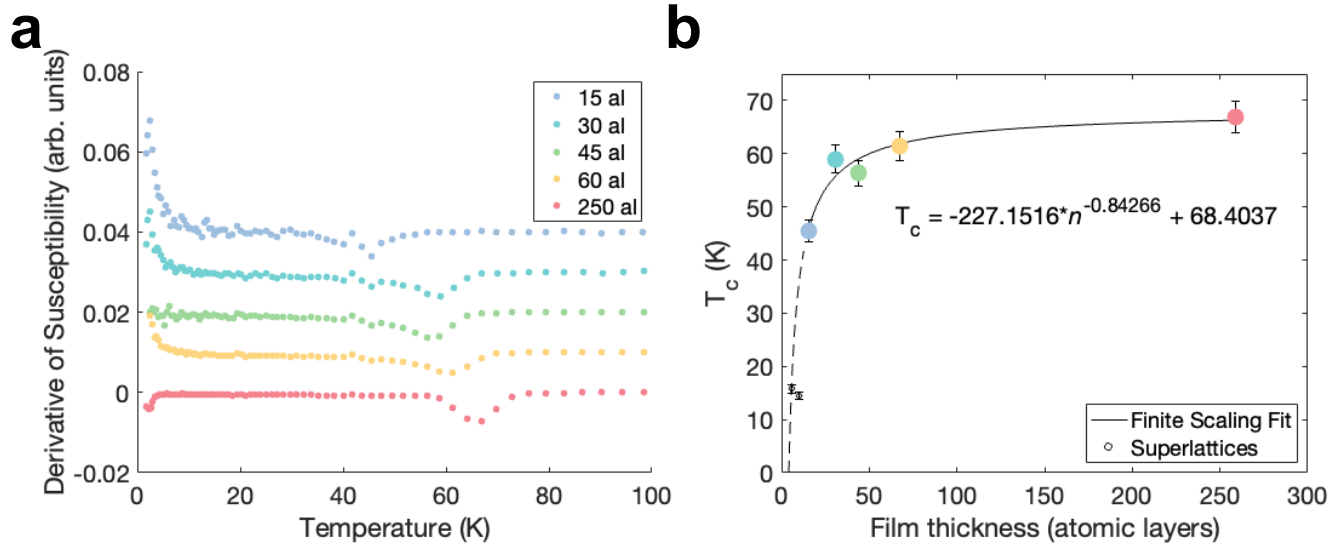


FIG. S30. Ferromagnetic transition temperatures of $Y_2V_2O_7$ thickness series in an out-of-plane field. **a** The derivatives of the magnetic susceptibilities measured in a magnetic field along ⟨111⟩ (plotted in lighter colors in Figure S29) **b** The ferromagnetic transition temperatures vs. film thicknes (n, atomic layers) in an out-of-plane magnetic field defined by the temperature where the magnetic susceptibility has the largest slope magnitude; all transition temperatures and the fit to finite size are consistent with the results in an in-plane field (Figure 2b)

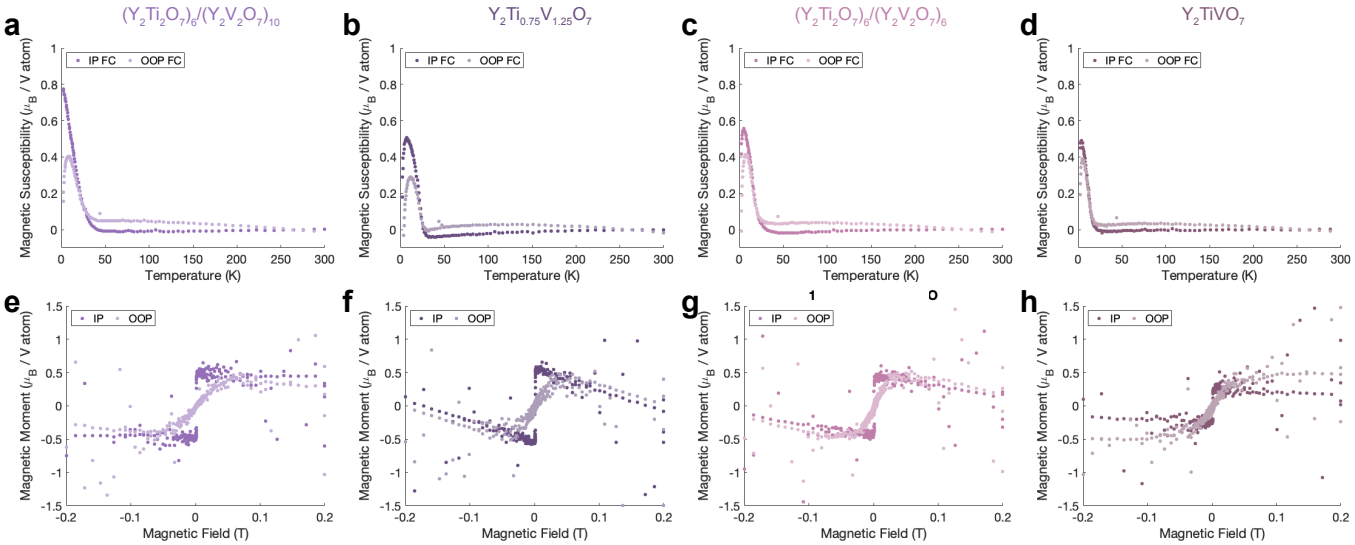


FIG. S31. Anisotropy of magnetism of $(Y_2Ti_2O_7)_6/(Y_2V_2O_7)_n$ superlattices. **a-d** Magnetic susceptiblity vs. temperature for a field applied within the plane of the film (IP, perpendicular to $\langle 111 \rangle$) and out-of-plane (OOP, along $\langle 111 \rangle$) for (a) $n = 10$, (b) the corresponding $Y_2Ti_{0.75}V_{1.25}O_7$, (c) $n = 6$, and (d) Y_2TiVO_7 **e-h** Magnetization vs. applied field loops at 10 K for a field applied in-plane and out-of-plane for the same films as the susceptibility above: (e) $n = 10$, (f) the corresponding $Y_2Ti_{0.75}V_{1.25}O_7$, (g) $n = 6$, and (h) Y_2TiVO_7

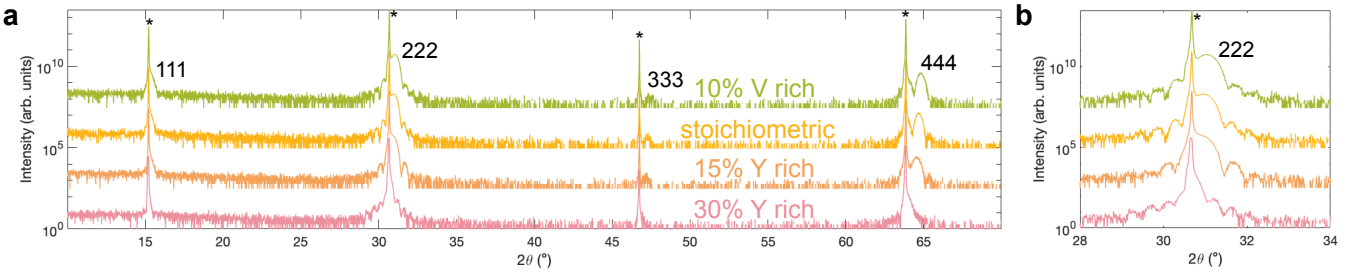


FIG. S32. X-ray diffraction of $Y_2V_2O_7$ on $Y_2Ti_2O_7$ with varying stoichiometry. **a** Full x-ray diffraction of a stoichiometry series of $Y_2V_2O_7$ showing a slight shifting of film peaks to higher angle with additional vanadium; asterisks indicate substrate diffraction peaks and lattice plane indices denote film peaks **b** Detail of 222 film peaks in (a)

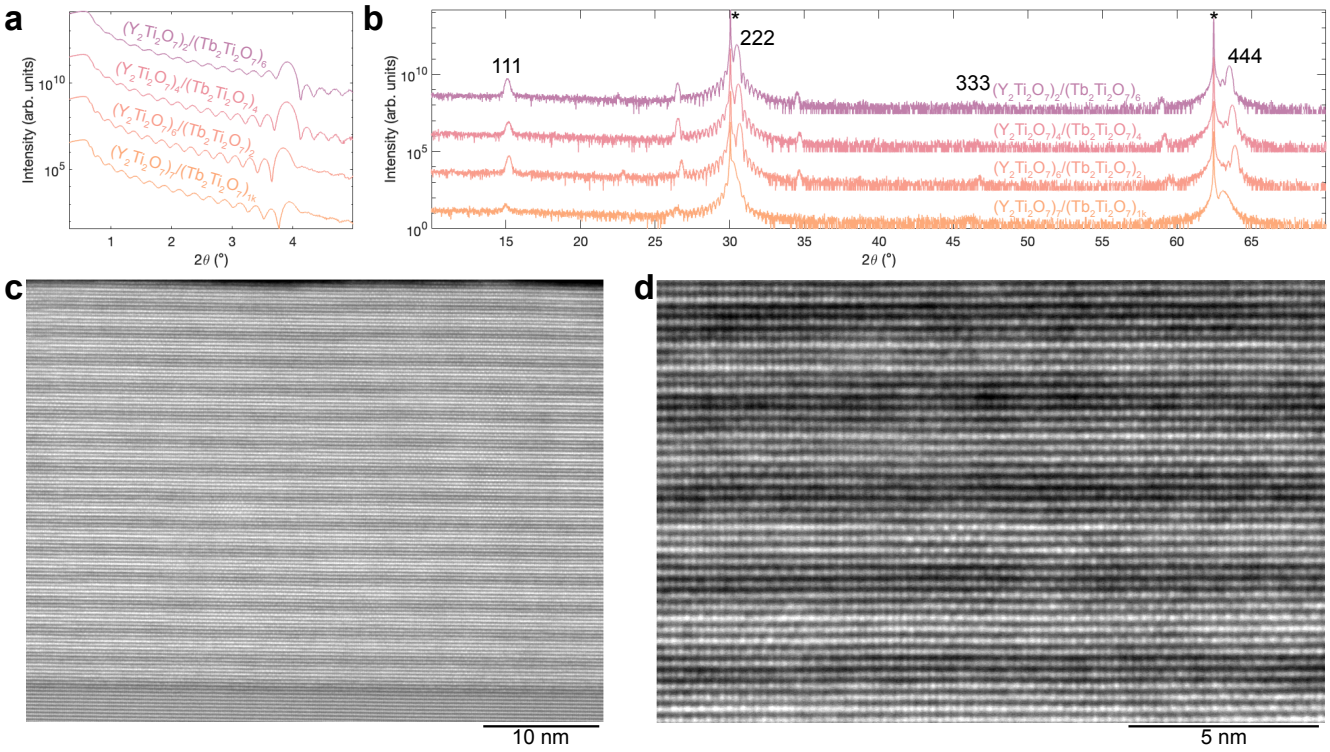


FIG. S33. Characterization of $(Y_2Ti_2O_7)_m/(Tb_2Ti_2O_7)_n$ superlattices as a proof-of-concept. **a** X-ray reflectivity of superlattices indicating a smooth film with a clear low angle superlattice peak with a symmetry that depends on m and n and a constant position because $m+n = 8$ for all films **b** X-ray diffraction showing high-quality pyrochlore films with clear superlattice satellite peaks about the typical pyrochlore peaks **c** A large field-of-view HAADF-STEM micrograph along $\langle 11\bar{2} \rangle$ with clear contrast between the $Tb_2Ti_2O_7$ layers (brighter) and $Y_2Ti_2O_7$ layers (dimmer) **d** A higher magnification view of (c) showing the superlattice layering in more detail